CRYSTAL GROWTH & DESIGN

pubs.acs.org/crystal

Article

Modeling the Composition of III−V Ternary Nanowires with Group V Depletion

Vladimir G. Dubrovskii*

Cite This: https://doi.org/10.1021/acs.cgd.4c01338

Read Online

ACCESS | Metrics & More | Article Recommendations

ABSTRACT: It is well documented that the concentrations of highly volatile group V atoms in liquid droplets catalyzing the vapor−liquid−solid growth of III−V nanowires decrease in the quasi-instantaneous process of monolayer progression and can even drop to equilibrium at a stopping size. This effect has far-reaching implications in the nanowire morphology, crystal phase, and nucleation statistics but was never considered in the compositional modeling of ternary nanowires. Here, we present the first attempt of such modeling for wurtzite III−V nanowires based on group V intermix. We show that the liquid−solid distribution of such nanowires starts from the kinetics shape at nucleation and transitions to the equilibrium distribution at the stopping size. The vapor−solid distribution is fully determined by the initial liquid composition at nucleation and is reduced to a simple analytic shape under some reasonable assumptions. When the stopping size is smaller than the nanowire monolayer, our theory predicts spatially inhomogeneous composition across the nanowire axis. The model fits very well the available compositional data on InP_xAs_{1-x}, GaP_xAs_{1-x}, and $InSb_xAs_{1-x}$ nanowires grown with different catalysts and sheds more light on the compositional control over III−V ternary nanowires in general. These results provide a starting point for further advancements in understanding and modeling of the complex growth process with a time-scale hierarchy of quasi-instantaneous monolayer progression and slow refill from vapor.

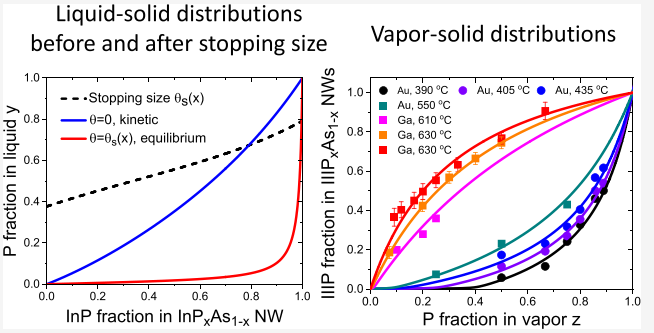

1. INTRODUCTION

Nanomaterials of different types offer much wider opportunities for bandgap engineering with widely tunable compositions compared to epi-layers.[1] In particular, III−V ternary nanowires (NWs) and heterostructures based on such NWs[2−5] allow for highly mismatched material combinations that can be grown on Si substrates.[3−7] This property is extremely promising for novel optoelectronic devices including lasers[8,9] and sources of nonclassical light.[10−12] Most freestanding III−V NWs are grown using the vapor−liquid−solid (VLS) method[13] with a liquid droplet (Au or a group III metal in the self-catalyzed VLS approach[14]). VLS III−V ternary NWs and NW heterostructures can be based either on group III[15−19] or group V[20−42] intermix (interchange). The latter case is much more complex due to high volatility of group V atoms causing their undetectable amounts in liquid. The stationary compositions of VLS III−V ternary NWs based on group intermix ($IIIV_xV_{1-x}$ NWs for brevity) under time-independent material fluxes and interfacial profiles in NW heterostructures under alternating fluxes were experimentally studied in different material systems including $InSb_xAs_{1-x}$,[20−23] $GaSb_xAs_{1-x}$,[24−28] InP_xAs_{1-x},[29−34] and GaP_xAs_{1-x}.[35−42] Among the most important experimental findings, it was shown that the vapor−solid distributions of Au-catalyzed InP_xAs_{1-x} NWs,[29] Au-catalyzed[39] and Ga-catalyzed[37,41] GaP_xAs_{1-x} NWs grown by different techniques are well-fitted by the one-parametric Langmuir-McLean (LM) formula.[43] The vapor−solid distributions of Au-catalyzed $InSb_xAs_{1-x}$ were found strongly dependent on the total V/III flux ratio,[20] and fitted by the model of Biefeld[44] with modified parameters.

These studies stimulated extensive theoretical research, reviewed in refs 45,46. According to the current view,[47−50] the stationary liquid−solid distributions are close-to-equilibrium[17,51−53] for VLS III−V NWs based on group III intermix, and kinetically limited[19,54] for VLS $IIIV_xV_{1-x}$ NWs. This important difference is due to extremely low concentrations of group V atoms in liquid in comparison with group III atoms that lead to group III rich conditions for liquid−solid growth.[47,50] The stationary vapor−solid distributions of VLS $IIIV_xV_{1-x}$ NWs, obtained in refs 48,49, circumvent the uncertainties in

Received: September 27, 2024
Revised: November 9, 2024
Accepted: November 19, 2024

the unknown liquid composition, and strongly depend on the total V/III ratio. These models fit reasonably well the available compositional data of refs 20,29,35,37,39,41. However, all the existing models for the liquid−solid and vapor−solid distributions of VLS III−V ternary NWs[47−49,51−54] use one simplifying assumption on the time-independent concentrations of different elements in liquid during the liquid−solid growth of ternary NW monolayer (ML). The validity of this assumption is not guaranteed even for group III atoms, and is definitely not true for group V atoms. Indeed, it is well-known that the ML progression in VLS NWs in general is quasi-instantaneous, that is, the ML growth is much faster than refill from vapor.[55−62] Therefore, the formation of single NW ML leads to significant depletion of a catalyst droplet with its group V atoms. This property has an important impact on the morphology and the related crystal phase,[56,57] sub-Poissonian nucleation statistics,[55,60] and length distributions[61,62] of VLS GaAs NWs.

In III−V NWs with small enough droplets and low enough initial concentrations of group V atoms, the liquid supersaturation may even drop to zero at a certain "stopping size" before the ML completion. This stopping effect was introduced in ref 63 in the field of NWs, but was earlier considered in connection with nucleation and growth in confined systems.[64−68] The effect was confirmed by in situ growth monitoring of NW growth inside a transmission electron microscope (TEM),[69−71] and has far reaching implication in the VLS growth and properties of III−V NWs [69−74]. According to ref 70, GaAs NWs form with planar liquid−solid interface, vertical sidewalls, and in the wurtzite (WZ) crystal phase in the intermediate range of the droplet contact angles from 100° to 125°. Larger contact angles yield the truncated geometry of the growth interface and the zincblende (ZB) crystal phase. The amount of truncation oscillates in synchronization with the ML growth cycle, reaching its maximum after the ML completion and minimum at nucleation.[56,57,70] The truncation can provide additional material to complete the NW ML, which is why the ML growth in ZB III−V NWs is always quasi-instantaneous. In WZ GaAs NWs, the truncation is suppressed on surface energetic grounds.[57,70] As a result, the ML progresses quasi-instantaneously only before reaching the stopping size, and then grows much slower at the rate of refill from vapor. This growth was described in detail in ref 72 for binary VLS III−V NWs. However, the effects of group V depletion and the time scale hierarchy in the ML growth before and after the stopping size was never considered for ternary III−V NWs.

This work tries to fill this gap by developing a model that takes into account the time dependences of group V concentrations in liquid during the VLS growth of WZ $\mathrm{III}V_xV_{1-x}$ NWs (or, more generally, NWs with planar liquid−solid interface). We show that the time scale hierarchy in the ML progression leads to new effects that affect very significantly the compositional trends. The stopping size at which the liquid supersaturation drops to zero always exists, because partial or full ML consumes the available group V atoms from liquid without refill from vapor. The presence or absence of the stopping effect in a given NW depends on whether the stopping size is smaller or larger than the full NW ML.[72] Consequently, the liquid−solid distribution of VLS $\mathrm{III}V_xV_{1-x}$ NWs is kinetic only at the very beginning of the ML growth, but then either reaches the equilibrium shape at the stopping size or approaches it with the ML progression. The stopping effect in NWs is size-dependent. This introduces nontrivial correlation between the radius, droplet angle and composition of VLS ternary NWs. Quasi-instantaneous ML growth before the stopping size is not affected by vapor. The NW composition in this stage depends only on the initial liquid composition at nucleation. Relating the latter to the vapor fluxes of group V atoms, we are able to derive the vapor−solid distribution of VLS $\mathrm{III}V_xV_{1-x}$ NWs, which is reduced to a simple analytic shape under some reasonable assumptions. On the other hand, slow ML growth after the stopping size is independent of the liquid state, which remains at equilibrium before the ML completion. Therefore, the vapor−solid distribution in the slow ML growth stage is determined by the vapor fluxes and desorption from equilibrium liquid. This difference naturally leads to spatial inhomogeneity of the composition across the NW axis. The model is validated against the available compositional data on $InSb_xAs_{1-x}$,[20] InP_xAs_{1-x}[29] and GaP_xAs_{1-x} NWs[35,37,39,41] NWs catalyzed by different droplets and grown by different epitaxy techniques. The most important result of the work is the first theoretical study of hierarchical growth of ternary MLs in VLS NWs, which can be translated to ternary NWs based on group III intermix, other material systems, catalyst-free growth techniques and different geometries of binary or pseudobinary nanostructures.

2. GROWTH MODEL

Consider a VLS ternary $A_xB_{1-x}C$ NW, with atoms A and B belonging to group V and atoms C belonging to group III. Spherical cap droplet resting on the NW top has the radius R and contact angle φ. The droplet volume is given by $V_{drop} = (\pi R^3/3)\Psi(\delta)$, with $\Psi(\delta)$ as the known geometrical function of the droplet contact angle δ (ref 72 The number of III−V pairs in a NW ML is given by $i_{ML} = CR^2h/\Omega_S$, with C as a shape constant (for example, $C = \pi$ for cylindrical NW) and Ω_S as the elementary volume per III−V pair in solid. A ternary NW is grown from a catalyst droplet fed by the total atomic fluxes of elements A, B and C, denoted ν_A, ν_B and ν_C, respectively. The numbers of atoms A and B in liquid equal l_A and l_B, respectively. The effective vapor composition Z and fraction of atoms A in liquid are defined according to

$$Z = \frac{\nu_A}{\nu_A + \nu_B},\ y = \frac{l_A}{l_A + l_B} \quad (1)$$

Considering that the vapor phase mainly consists of group V dimers A_2 and B_2, at least in the case of molecular beam epitaxy (MBE),[48,49,75] the arrival rates of atoms A and B are given by $\nu_A = 2\sigma_A I_{A_2}\pi R^2\gamma(\delta)$ and $\nu_B = 2\sigma_B I_{B_2}\pi R^2\gamma(\delta)$. Here, I_{k_2} are the vapor fluxes of $k = A, B$ dimers, $\gamma(\delta)$ is a geometrical function of the droplet contact angle,[48,49,75] and σ_k summarize the effects of (i) possibly different adsorption coefficients of $k = A, B$ species on the droplet surface,[29,37,39] (ii) different re-emission of group V species from the surrounding surfaces,[75] and (iii) different surface diffusion of atoms A and B from the NW sidewalls to the droplet over a short distance.[76,77] As a result, the fraction of atoms A in vapor z is related to the effective vapor composition Z by the LM equation[43]

$$z = \frac{I_{A_2}}{I_{A_2} + I_{B_2}} = \frac{Z}{Z + c_g(1 - Z)},\ c_g = \frac{\sigma_A}{\sigma_B} \quad (2)$$

where the kinetic coefficient c_g describes different transport of atoms A and B into the droplet. Obviously, $z = Z$ only when $c_g = 1$. The concentrations of atoms A and B in liquid are given by

https://doi.org/10.1021/acs.cgd.4c01338
Cryst. Growth Des. XXXX, XXX, XXX−XXX

$$\chi_k = \frac{l_k}{l_{tot}},\ l_{tot} = \frac{1}{\Omega_L}\frac{\pi R^3}{3}\Psi(\delta) \cong const,\ k = A,\ B \tag{3}$$

where Ω_L is the effective elementary volume per atom in liquid. The total number of all atoms in liquid $l_{tot} = l_C + l_{Au} + l_A + l_B \cong l_C + l_{Au}$ (with l_C and l_{Au} as the numbers of group III atoms C and Au atoms in the droplet, respectively) can be considered time-independent due to $\chi_A \ll 1$ and $\chi_B \ll 1$.

In what follows, we consider time-dependent l_k that account for the effect of group V depletion due to ML growth. In this case, the numbers of atoms A and B (or pairs AC and BC) i_A and $i_B$in two-dimensional (2D) island or partial ML also depend on time. Therefore, definition of the solid composition requires some care. We define the time-dependent (or coordinate-dependent) solid composition x according to

$$x = \frac{di_A/dt}{di_A/dt + di_B/dt} = \frac{di_A}{di},\ i = i_A + i_B \tag{4}$$

as in the kinetic models of refs 45−50,54. Here, di_k/dt are the growth rates of binaries AC and BC. These rates are entirely determined by the attachment-detachment rates of highly volatile group V atoms A and B due to their low concentrations in the droplet ($\chi_A \ll \chi_C, \chi_B \ll \chi_C$).[47] The total number of III−V pairs in partial ML i changes from $i \cong 0$ at nucleation (due to a small critical size consisting of only a few III−V pairs[53,75]) to i_{ML} after the ML completion. The solid composition defined by eq 4 depends on the size of partial ML i. The average solid composition at a given i is determined by

$$\overline{x} = \frac{1}{i}\int_0^i di'\frac{di_A}{di'} = \frac{i_A}{i} = \frac{i_A}{i_A + i_B} \tag{5}$$

and is different from x in the general case. From eqs 4 and 5, it is easy to obtain

$$\frac{d\overline{x}}{dt} = \frac{1}{i}\left[(1-\overline{x})\frac{di_A}{dt} - \overline{x}\frac{di_B}{dt}\right] = \frac{x-\overline{x}}{i} \tag{6}$$

showing that the solid composition is spatially homogeneous only when $x = \overline{x}$ for any i.

Our growth model generalizes the approach of ref 72 to the case of VLS ternary $IIIV_xV_{1-x}$ NWs with planar liquid−solid interface. The growth rates of binaries AC and BC in partial ternary ML must be proportional to the differences between the time-dependent l_k and the equilibrium numbers of atoms $k = A, B$ in liquid $l_{k,\,eq}$:

$$\frac{di_A}{dt} = \frac{W}{\tau_A}(l_A - l_{A,eq}),$$
$$\frac{di_B}{dt} = \frac{W}{\tau_B}(l_B - l_{B,eq}) \tag{7}$$

Here, the function $W(i, R, \delta)$ depends on the mechanisms of material transport from liquid to solid, but should be the same for atoms A and B.[47,54] The characteristic times τ_A and τ_B may be, however, different due to different diffusion coefficients of atoms A and B in liquid.[47−49,54] The numbers of atoms A and B in liquid change with time due to ML growth, refill at the rates ν_k and desorption from the droplet surface:

$$\frac{dl_A}{dt} = -\frac{di_A}{dt} + \nu_A - \nu_A^{des}e^{2\psi_A}\left(\frac{l_A}{l_{tot}}\right)^2,$$
$$\frac{dl_B}{dt} = -\frac{di_B}{dt} + \nu_B - \nu_B^{des}e^{2\psi_B}\left(\frac{l_B}{l_{tot}}\right)^2 \tag{8}$$

The equilibrium quantities $l_{k,\,eq}$ are x−dependent due to binary interactions between dissimilar AC and BC pairs in solid:[44−54]

$$l_{A,eq}(x) = l_{tot}\frac{e^{-\Delta\mu_{AC}^p - \psi_A - \psi_c}}{\chi_C}xe^{\omega(1-x)^2},$$
$$l_{B,eq}(x) = l_{tot}\frac{e^{-\Delta\mu_{BC}^p - \psi_B - \psi_c}}{\chi_C}(1-x)e^{\omega x^2} \tag{9}$$

with $\chi_C \cong 1 - \chi_{Au} \cong const$. The functions ψ_k in the above equations describe the interaction terms in the chemical potentials of group V atoms A, B and group III atoms C in liquid, given by $\mu_A^l = \mu_A^{l,p} + ln\,\chi_A + \psi_A$, $\mu_B^l = \mu_B^{l,p} + ln\,\chi_B + \psi_B$, and $\mu_C^l = \mu_C^{l,p} + ln\,\chi_C + \psi_C$. The quantities $\mu_k^{l,p}$ denote the chemical potentials of pure k = A, B and C liquids, and $\mu_{kC}^{s,p}$ are the chemical potentials of solid binaries AC and BC. The quantities $\Delta\mu_{AC}^p = \mu_A^{l,p} + \mu_C^{l,p} - \mu_{AC}^{s,p}$ and $\Delta\mu_{BC}^p = \mu_B^{l,p} + \mu_C^{l,p} - \mu_{BC}^{s,p}$ denote the chemical potential differences for pure binaries. All these chemical potentials are expressed in thermal units. With neglect of small corrections, the interaction terms ψ_k are determined by χ_C and independent of χ_A and χ_B. This will be discussed in more detail below. With the known l_A^0, l_B^0, or the initial liquid composition $y_0 = l_A^0/l_{tot}^0$ and the total number of atoms A and B in liquid $l_{tot}^0 = l_A^0 + l_B^0$ at nucleation, the ML growth kinetics and depletion of group V atoms A and B in liquid in each ML growth cycle (including refill) are fully described by eqs 7 and 8.

According to the in situ TEM data[56,57,69,70,73] and theoretical considerations,[55,60,61,63,72−74] the ML progression before the stopping size is much faster than refill from vapor. This corresponds to $\nu_A\tau_A \ll 1$, $\nu_B\tau_B \ll 1$ in eqs 7 and 8. Using this time-scale hierarchy, we can use $l_A \cong l_A^0$ and $l_B \cong l_B^0$ in eqs 7, meaning that partial ML evolves quasi-instantaneously in the absence of any refill before reaching the stopping size

$$i_s(x) = l_A^0 + l_B^0 - l_{A,eq}(x) - l_{B,eq}(x) \tag{10}$$

This generalizes the result of ref 72 for ternary ML. In this case, the stopping size depends on the ML composition x. More precisely, the stopping size is affected by the composition of the NW "core" that forms in the fast ML growth stage. If the stopping size at a given composition x is larger than the ML size ($i_s(x) > i_{ML}$), the whole ML grows quasi-instantaneously. In the opposite case of $i_s(x) < i_{ML}$, partial ML evolves quasi-instantaneously only before reaching the stopping size, where the liquid supersaturation drops to zero. In the absence of material supply from the truncation (as in WZ GaAs NWs[69,70,72−74]) further ML growth occurs much slower at the rate of refill. The liquid phase stays at equilibrium before the ML completion, and then rises to the initial level at nucleation. After that, the whole ML growth cycle is repeated. This picture is well-known for binary VLS III−V NWs.[63,72−74] However, such a hierarchical ML growth was never considered for ternary MLs. In what follows, we study this process in detail and reveal the influence of the group V depletion on the compositional trends in VLS $IIIV_xV_{1-x}$ NWs.

https://doi.org/10.1021/acs.cgd.4c01338
Cryst. Growth Des. XXXX, XXX, XXX−XXX

The growth and compositional modeling based on eqs 7 and 8 requires knowledge on the characteristic growth times τ_A and τ_B entering eq 7, or at least their ratio $c_l = \tau_B/\tau_A$. The constant c_l describes different transport of atoms A and B through liquid, and enters the existing kinetic models for the NW composition in the stationary approach.[19,47−49,54] Unfortunately, however, the quantities τ_A, τ_B and c_l remain largely unknown. Direct measurements of the characteristic times τ_k is difficult even using in situ TEM monitoring of binary NW growth, because the ML progression is too fast to be quantified.[56,69,73] Some models earlier assumed that $c_l = 1$.[19,54] It is clear that the characteristic growth times are proportional to the diffusion coefficients of group V atoms A and B in an Au-group III melt: $1/\tau_A \propto D_{A,\,eff}/\Omega_L^{2/3}$, $1/\tau_B \propto D_{B,\,eff}/\Omega_L^{2/3}$. Let us consider the macroscopic Stokes−Einstein formula for $D_{k,\,eff}$ (ref 78):

$$D_{k,eff} = \frac{k_B T}{6\pi\eta r_k} \tag{11}$$

where T is the absolute temperature, k_B is the Boltzmann constant, η is the liquid viscosity, and r_k is the radius of a diffusing spherical particle. If we apply this relation for atoms, η depends only on χ_c and is not affected by atoms A and B due to their negligible amount in liquid. Then, the only difference in the diffusion coefficients is due to different atomic radii of group V atoms r_k, which equal 0.148 nm for As, 0.134 nm for P, and 0.161 for Sb.[79] These values are very close, which justifies the assumption of $c_l \cong 1$. In what follows, we will use this assumption corresponding to

$$\tau_A = \tau_B = \tau \tag{12}$$

in eqs 7. The case $c_l \neq 1$ is more complex and will be studied elsewhere.

3. GROWTH CYCLE OF TERNARY MONOLAYER

In the *fast ML growth stage*, which occurs for the whole ML at $i_s > i_{ML}$ or for partial ML before reaching the stopping size at $i_s < i_{ML}$, eqs 7 and 8 at $\tau_A = \tau_B = \tau$ and $\nu_k\tau \ll 1$ for both atoms A and B are reduced to

$$\frac{di_A}{dt} = \frac{W}{\tau}(l_A^0 - l_{A,eq}),\ \frac{di_B}{dt} = \frac{W}{\tau}(l_B^0 - l_{B,eq}),$$
$$l_A = l_A^0 - i_A,\ l_B = l_B^0 - i_B \tag{13}$$

These equations describe quasi-instantaneous growth of the numbers of pairs AC and BC in partial ML to their maximum values $l_k^0 - l_{k,\,eq}$, and the corresponding depletion of a catalyst droplet with its atoms A and B in the absence of refill. When W is independent of the island size i ($W = 1$),[72] eqs 13 are analytically resolved:

$$i_k = (l_k^0 - l_{k,eq})(1 - e^{-t/\tau}),$$
$$l_k = l_k^0 - (l_k^0 - l_{k,eq})(1 - e^{-t/\tau}),\ k = A, B \tag{14}$$

In this model, the numbers of pairs AC and BC in solid exponentially increase to $l_k^0 - l_{k,\,eq}$, whereas the numbers of atoms A and B in liquid exponentially decrease to their equilibrium values $l_{k,\,eq}$, with a characteristic time constant τ. Using eqs 13 and 14 in eqs 4 for x and 5 for $\overline{x}$, it is seen that the local and average composition of partial ML before the stopping size equal each other:

$$x = \overline{x} = \frac{l_A^0 - l_{A,eq}(x)}{l_A^0 - l_{A,eq}(x) + l_B^0 - l_{B,eq}(x)} \tag{15}$$

The composition-dependent equilibrium functions $l_{k,\,eq}(x)$ are given by eqs 9. The composition-dependent stopping size is given by eq 10. For any ML size i, the numbers of AC and BC pairs equal $i_A = xi$, $i_B = (1 - x)i$, with $i = i_s(x)[1-\exp(-t/\tau)]$. The total number of group V atoms in liquid decreases as $l_A + l_B = l_A^0 + l_B^0 - i$, and tends to the x−dependent equilibrium value $l_{A,\,eq}(x) + l_{B,\,eq}(x)$ at the stopping size. When W in eqs 7 depends on the island size i (for example, $W \propto i^{1/2}$ if the binary growth rates are proportional to the island perimeter[47,75]), the ML growth kinetics becomes more complex. However, the prefactor W cancels in the ratio of di_A/dt over di/dt in eq 4 for x. Consequently, we have $x = \overline{x}$ given by eq 15 provided that $\tau_A = \tau_B$.

When the stopping size for a given composition is smaller than the ML size, the fast ML growth stage occurs for $0 \le i \le i_s(x)$. After reaching the stopping at the moment of time $t_1 \sim \tau$, further ML growth requires refill from vapor. The *slow ML growth stage* occurs at the time-independent $l_A = l_{A,\,eq}(x)$ and $l_B = l_{B,\,eq}(x)$. This growth is described by eqs 8 at $dl_A/dt = dl_B/dt = 0$:

$$\frac{di_A}{dt} = \nu_A - \nu_A^{des} e^{2\psi_A}\left(\frac{l_{A,eq}(x)}{l_{tot}}\right)^2,$$
$$\frac{di_B}{dt} = \nu_B - \nu_B^{des} e^{2\psi_B}\left(\frac{l_{B,eq}(x)}{l_{tot}}\right)^2 \tag{16}$$

Using these binary growth rates in eq 4 leads to a time-independent solution for x, which is, however, different from the average composition $\overline{x}$. This will be discussed in detail later on. Integration of eqs 16 at $x = const$ yields the linear increase of the ML size with time

$$i = i_s(x) + \left[\nu_A - \nu_A^{des} e^{2\psi_A}\left(\frac{l_{A,eq}(x)}{l_{tot}}\right)^2 + \nu_B - \nu_B^{des} e^{2\psi_B}\left(\frac{l_{B,eq}(x)}{l_{tot}}\right)^2\right](t - t_1) \tag{17}$$

The ML growth is completed when i reaches the ML size i_{ML} at the moment of time t_2:

$$t_2 - t_1 \cong t_2 = \frac{i_{ML} - i_s(x)}{\nu_A - \nu_A^{des} e^{2\psi_A}(l_{A,eq}(x)/l_{tot})^2 + \nu_B - \nu_B^{des} e^{2\psi_B}(l_{B,eq}(x)/l_{tot})^2} \tag{18}$$

The slow ML growth stage occurs for $i_s(x) < i \le i_{ML}$ and ends at the moment of time t_2.

After the ML completion ($i = i_{ML}$), the *refill stage* is described by eqs 8 at $di_A/dt = di_B/dt = di/dt = 0$:

$$\frac{di_A}{dt} = \nu_A - \nu_A^{des} e^{2\psi_A}\left(\frac{l_A}{l_{tot}}\right)^2,$$
$$\frac{l_B}{l_{tot}} = \nu_B - \nu_B^{des} e^{2\psi_B}\left(\frac{l_B}{l_{tot}}\right)^2 \tag{19}$$

with the initial conditions $l_k(t = t_2) = l_k^{eq}(x)$. The solutions for the liquid composition are given by

https://doi.org/10.1021/acs.cgd.4c01338
Cryst. Growth Des. XXXX, XXX, XXX−XXX

$$\frac{l_A}{l_{A,s}} = th\left[\frac{t - t_2}{t_A} + arcth\left(\frac{l_{A,eq}(x)}{l_{A,s}}\right)\right],$$

$$\frac{l_B}{l_{B,s}} = th\left[\frac{t - t_2}{t_B} + arcth\left(\frac{l_{B,eq}(x)}{l_{B,s}}\right)\right] \quad (20)$$

Here, the characteristic times t_k and the maximum numbers of atoms A and B in liquid $l_{k,s}$ equal

$$\frac{1}{t_A} = \frac{1}{l_{tot}}\sqrt{\nu_A \nu_A^{des}}\, e^{\psi_A},\ \frac{1}{t_B} = \frac{1}{l_{tot}}\sqrt{\nu_B \nu_B^{des}}\, e^{\psi_B},$$

$$l_{A,s} = l_{tot}\sqrt{\frac{\nu_A}{\nu_A^{des}}}\, e^{-\psi_A} = \nu_A t_A,\ l_{B,s} = l_{tot}\sqrt{\frac{\nu_B}{\nu_B^{des}}}\, e^{-\psi_B} = \nu_B t_B \quad (21)$$

At $l_k = l_{k,s}$, the incoming fluxes of group V atoms ν_k are compensated by their desorption from liquid. The refill stage continues from the moment of time t_2 to t_{ML}. At the end of the ML growth cycle (ML growth and refill), the liquid must resume its initial composition at nucleation. Therefore, we have

$$\frac{l_k^0}{l_{k,s}} = th\left[\frac{t_{ML} - t_2}{t_k} + arcth\left(\frac{l_{k,eq}(x)}{l_{k,s}}\right)\right],\ k = A, B \quad (22)$$

showing that the maximum contents of group V elements A and B in liquid are reached at $t_{ML} - t_2 \sim t_k$.

It is convenient to present the ML growth kinetics in terms of the ML coverage $\theta = i/i_{ML}$, which changes from 0 to 1 in the ML growth step.[72] The coverages $\theta_k = i_k/i_{ML}$ correspond to AC and BC binaries in ternary ML. The stopping size becomes $\theta_s(x) = i_s(x)/i_{ML}$, and the presence or absence of the stopping effect at a given NW composition depends on whether $\theta_s(x) < 1$ or $\theta_s(x) > 1$. The effective coverages in liquid become $\theta_{k,l} = l_k/i_{ML}$, with $\theta_{k,l}^0 = l_k^0/i_{ML}$ as the initial coverages at nucleation. Figure 1 shows the time-dependent θ_k, θ and $\theta_{k,l}$ for a ternary NW with $W = 1$, $t_{ML} = 8$ s, $\tau = 0.05$ s, $\theta_{A,l}^0 = 0.1$ ML, $\theta_{B,l}^0 = 0.4$ ML, $\theta_{A,l}^{eq} = 0.02$ ML, $\theta_{B,l}^{eq} = 0.08$ ML, $\nu_A/i_{ML} = 0.4$ ML/s, $\nu_B/i_{ML} = 0.1$ ML/s, $t_A = 2$ s and $t_B = 3$ s. The curves are obtained from eqs 14 in the fast ML growth stage, (16) in the slow ML growth stage, and (20) in the refill stage. With these model parameters, the stopping size $\theta_s(x)$ equals 0.4 ML. Partial $A_xB_{1-x}C$ ML as a whole, as well as its binary fractions AC and BC, evolve quasi-instantaneously to the stopping size. The fast ML growth stage ends up at 0.2 s after nucleation. The follow-up slow ML growth continues at the rates of refill, with negligible desorption. This stage ends up at 1.45 s after nucleation. The longest stage in this example is refill, because the effective liquid coverages at nucleation $\theta_{A,l}^0$ and $\theta_{B,l}^0$ are very close to the stationary values $\theta_{A,s} = l_{A,s}/i_{ML}$ and $\theta_{B,s} = l_{B,s}/i_{ML}$. The composition of partial ML equals 0.2 before and 0.8 after the stopping size. This example shows that the composition of $IIIV_xV_{1-x}$ NWs with a stopping size is generally expected to be inhomogeneous across the NW axis. This is not exactly a core–shell structure, because MLs in WZ III–V NWs start from the triple phase line at the NW perimeter[80] or even at the edges of hexahedral NW.[69] This effect will be discussed in more detail below.

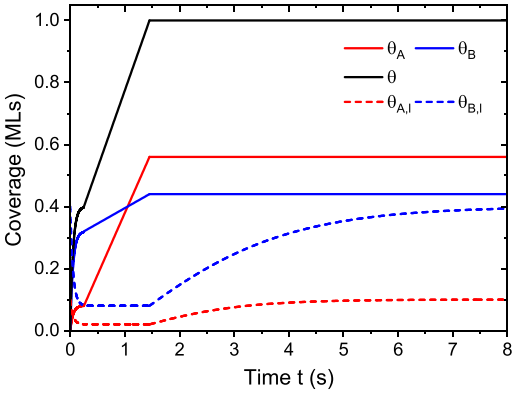

Figure 1. Growth cycle of ternary ML in an $A_xB_{1-x}C$ NW with a stopping size of 0.4 ML and spatially inhomogeneous composition x of 0.2 before and 0.8 after the stopping size. The binary ML coverages θ_k and the full ML coverage θ are shown by solid lines. The effective liquid coverages $\theta_{k,l}$ are shown by dashed lines. Separation of the ML growth cycle into the fast ML growth stage until the stopping size, slow ML growth stage until the ML completion, and even slower refill stage is clearly seen.

4. LIQUID–SOLID DISTRIBUTIONS

According to the results of the previous section, the liquid–solid distribution $y(x)$ connecting the composition of solid NW x and the liquid composition y is relevant only in the fast ML growth stage. Indeed, partial ML is fed from liquid only in the fast growth stage. As discussed in ref 72 for binary III–V NWs, the numbers of group V atoms in the droplet are proportional to the droplet volume (R^3), whereas the ML size is proportional to R^2. Hence, the stopping effect is more probable in thinner NWs, and at lower initial group V concentrations in their droplets. Without any stopping effect, the fast ML growth stage continues before the ML completion, and the liquid–solid distribution is relevant for any ML size. However, in NWs with a stopping size, partial ML grows directly from vapor at $i > i_s$. The liquid phase simply stays at equilibrium in the slow ML growth stage and has no influence on the NW composition. The latter is affected only by the vapor fluxes ν_k and probably by desorption from equilibrium liquid, which is the same as desorption from solid.

Furthermore, our eq 15 shows that the solid composition in the fast ML growth stage depends only on the initial numbers (or initial concentrations) of atoms A and B in liquid l_A^0 and l_B^0 (or χ_A^0 and χ_B^0). This is not surprising because, in the absence of refill, the liquid and solid compositions are related by

$$x = y - \frac{l_{A,eq}(x)}{l_A^0 + l_B^0 - i} \quad (23)$$

This relationship follows directly from eqs 13, with $y = l_A/(l_A + l_B)$ as the current liquid composition at the ML size i. Therefore, the standard view on the liquid–solid distributions of ternary III–V NWs at a time-independent (or size-independent) liquid state[45−49,54] must be refined in the following way. The relevant liquid–solid distribution in the fast ML growth stage connects the initial liquid composition at nucleation $y_0 = l_A^0/(l_A^0 + l_B^0)$ and the ML composition in this stage x. This distribution is easily obtained from eq 15:

$$y_0 = x + \frac{(1 - x)l_{A,eq}(x) - xl_{B,eq}(x)}{l_A^0 + l_B^0} \quad (24)$$

Using eq 23, the deterministic liquid–solid distribution connecting the liquid composition at the ML size i with the same solid composition x is obtained in the form

https://doi.org/10.1021/acs.cgd.4c01338
Cryst. Growth Des. XXXX, XXX, XXX−XXX

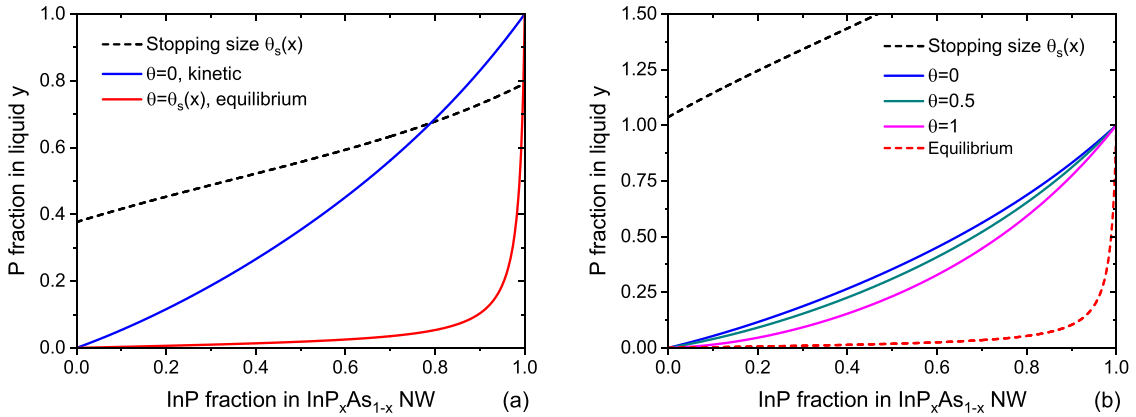

Figure 2. Liquid−solid distributions of self-catalyzed InP_xAs_{1-x} NWs at 450 °C at different ML coverages θ (a) with and (b) without the stopping effect (solid lines). The composition-dependent stopping size, shown by black dashed lines, is smaller than unity in (a) and larger than unity in (b) for all x. The kinetic liquid−solid distributions at nucleation ($\theta = 0$) are the same in both cases. The liquid−solid distribution in (a) reaches the equilibrium shape at the stopping size, while the curves in (b) are quite similar for all θ from 0 to 1, and far from the equilibrium shape (red dashed line).

$$y = x + \frac{(1-x)l_{A,eq}(x) - xl_{B,eq}(x)}{l_A^0 + l_B^0 - i}, \; . \; 0 \le i \le i_s(x) \tag{25}$$

This distribution becomes equilibrium at $i = i_s(x)$:

$$y_s = y_{eq} = \frac{l_{A,eq}(x)}{l_{A,eq}(x) + l_{B,eq}(x)} \tag{26}$$

This result is anticipated, because the stopping size is reached when liquid is at equilibrium with solid.

Using eqs 9 for x−dependent $l_{k,\,eq}(x)$, the obtained expressions can be presented in the standard notations.[45−49,51−54] The stopping size given by eq 10 becomes

$$i_s(x) = (l_A^0 + l_B^0)[1 - \Gamma_l(xe^{\omega(1-x)^2} + \beta_l(1-x)e^{\omega x^2})] \tag{27}$$

Here, the parameter Γ_l is inversely proportional to the liquid−solid binary supersaturation for AC pairs, and β_l is the parameter related to the affinity, or thermodynamic stability of AC over BC pairs in liquid:

$$\Gamma_l = \frac{e^{-\Delta\mu_{AC}^p - \psi_A - \psi_C}}{(\chi_A^0 + \chi_B^0)\chi_C}, \; \beta_l = e^{\Delta\mu_{AC}^p - \Delta\mu_{BC}^p + \psi_A - \psi_B} \tag{28}$$

Equations 24 to 26 take the form

$$y_0 = x + \Gamma_l g(x),$$

$$y = x + \Gamma_l \frac{g(x)}{1 - i/(l_A^0 + l_B^0)},$$

$$y_s = y_{eq} = \frac{x}{x + \beta_l(1-x)e^{\omega(2x-1)}} \tag{29}$$

Here, the kinetic function $g(x)$ is given by

$$g(x) = x(1-x)[e^{\omega(1-x)^2} - \beta_l e^{\omega x^2}] \tag{30}$$

The kinetic liquid-distribution of VLS $IIIV_xV_{1-x}$ NWs in eq 29 for y_0 is the same as in refs 47,54 at $c_l = 1$, but applies only to the initial liquid composition. The total number of group V atoms in liquid at nucleation, or their total concentration $\chi_A^0 + \chi_B^0$ entering the obtained liquid−solid distributions cannot be determined by considering the liquid−solid growth alone. Its determination requires additional treatment of the refill stage, and will be discussed in the next section.

Figures 2 show the evolution of the liquid−solid distributions of self-catalyzed InP_xAs_{1-x} NWs at 450 °C. The curves are obtained from eqs 27 to 30 with $\omega = 0.485$ and $\beta_l = 52.9$[81,82] at a fixed Γ_l of 0.01 and two different $\theta_{A,\,l}^0 + \theta_{B,\,l}^0$=0.8 and 2.2. This corresponds, for example, to thin and thick NWs with otherwise identical parameters. In the first case, the stopping size is smaller than unity for all x. Consequently, the initially kinetic liquid−solid distribution transitions to the equilibrium shape at the stopping size. In the second case, the stopping size is larger than unity for all x, which is why the distributions are close-to-kinetic for all θ from zero to unity. This justifies the earlier assumption of a time-independent liquid composition,[45−50,54] but only for NWs without the stopping effect.

5. VAPOR−SOLID DISTRIBUTIONS

According to the results of the previous section, the NW composition after the stopping size is determined by eq 16 for the growth rates of binaries AC and BC, which contain no characteristics of atoms A and B in liquid. Using these expressions in eq 4, it is easy to obtain the vapor−solid distribution in the form

$$Z = x + \Gamma_g f(x), \; i > i_s(x),$$

$$f(x) = x(1-x)[xe^{2\omega(1-x)^2} - \beta_g(1-x)e^{2\omega x^2}],$$

$$\Gamma_g = \frac{\nu_A^{des}}{\nu_A + \nu_B}\frac{e^{-2\Delta\mu_{AC}^p - 2\psi_C}}{\chi_C^2}, \; \beta_g = \frac{\nu_B^{des}}{\nu_A^{des}}e^{2(\Delta\mu_{AC}^p - \Delta\mu_{BC}^p)} \tag{31}$$

The analytic form of this vapor−solid distribution is similar to the liquid−solid distribution given by eqs 29 and 31. However, the kinetic function $f(x)$ is different from $g(x)$. The "supersaturation" parameter Γ_g and the affinity parameter β_g contains the total flux $\nu_A + \nu_B$ and the desorption rates of A and B atoms rather than interactions of different atoms in liquid. The characteristics of liquid remaining in the parameter Γ_g (χ_C and ψ_C) depend only on the percentage of Au in the droplet. In particular, $\psi_C \cong 0$ at $\chi_C \cong 1$ for self-catalyzed VLS growth.

The vapor−solid distributions of VLS $IIIV_xV_{1-x}$ NWs before the stopping size should be determined from the liquid−solid distribution given by eq 29 for y_0, where the unknown liquid

https://doi.org/10.1021/acs.cgd.4c01338
Cryst. Growth Des. XXXX, XXX, XXX−XXX

composition y_0 and the total concentration of group V atoms $\chi_A^0 + \chi_B^0$ should be expressed through the vapor fluxes of atoms A and B and their desorption rates.[47−49] This should be done using eq 22 at the end of the ML growth cycle. Determination of the duration of the whole ML growth cycle t_{ML} in these expressions requires, however, some additional considerations, such as the nucleation rate on the top facet in the mononuclear growth regime,[73−75] or group III based NW growth rate.[48,49] Regardless of the nature of t_{ML}, our model contains two distinct VLS growth regimes of $IIIV_xV_{1-x}$ NWs.

In *regime 1 with negligible desorption rates*, the characteristic times t_k are much longer than t_{ML}:

$$\frac{t_{ML}}{t_A} \ll 1, \frac{t_{ML}}{t_B} \ll 1 \tag{32}$$

In this case, the group V concentrations at nucleation are much smaller than their stationary values: $l_A^0 \ll l_{A,s}$, $l_B^0 \ll l_{B,s}$. In such a regime, both group V fractions in liquid increase linearly with time in the refill stage, with negligible desorption. Therefore, we have $l_A^0 = l_{A,eq}(x) + \nu_A(t_{ML} - t_2)$, $l_B^0 = l_{B,eq}(x) + \nu_B(t_{ML} - t_2)$. Negligible desorption in the refill stage allows one to omit the desorption terms in eqs 16 to 18, which apply to a shorter ML growth stage after the stopping size. Then the ML formation time t_2 and the total duration of the ML growth cycle including refill are given by

$$t_2 = \frac{i_{ML} - i_s(x)}{\nu_A + \nu_B}, \quad t_{ML} = \frac{i_{ML}}{\nu_A + \nu_B} \tag{33}$$

This result is not surprising, because in the regimes with negligible desorption (for example, at a low temperature of ~400 °C for self-catalyzed binary GaAs NWs[72]), the ML growth cycle is simply determined by the incoming fluxes of group V atoms. At nucleation ($t = 0 = t_{ML}$), we have $Zi_s(x) = l_A^0 - l_{A,eq}(x)$, $(1 - Z)i_s(x) = l_B^0 - l_{B,eq}(x)$, and hence

$$y_0 = Z + \frac{(1 - Z)l_{A,eq}(x) - Zl_{B,eq}(x)}{l_A^0 + l_B^0} \tag{34}$$

Comparing this result for y_0 with eq 29, we obtain

$$Z = x \tag{35}$$

In regime 1, this result applies uniformly for any ML size regardless of the presence or absence of the stopping effect. This can be understood as follows. No group V atoms can be lost from a catalyst droplet in the fast ML growth stage before the stopping size or up to the full ML. Without desorption, no group V atoms can be lost in the slow ML growth stage after the stopping size if it exists. After the ML completion, no group V atoms leave the droplet by desorption in the refill stage. Consequently, the composition of $IIIV_xV_{1-x}$ NW is entirely determined by the incoming fluxes of atoms A and B, as given by eq 35. This vapor−solid distribution is not affected by the values of l_A^0 and l_B^0 at nucleation, and is totally independent of the liquid state.

Regime 2 with high desorption rates occurs when the characteristic times t_k are much longer than t_{ML}:

$$\frac{t_{ML}}{t_A} \gg 1, \frac{t_{ML}}{t_B} \gg 1 \tag{36}$$

This regime corresponds to slow NW growth rates. Nucleation of MLs occurs at group V concentrations that are very close to their stationary values:

$$l_A^0 = l_{A,s} = l_{tot}\sqrt{\frac{\nu_A + \nu_B}{\nu_A^{des}}}\, e^{-\psi_A}\sqrt{Z}, \; l_B^0 = l_{B,s} = l_{tot}\sqrt{\frac{\nu_A + \nu_B}{\nu_B^{des}}}\, e^{-\psi_B}\sqrt{1 - Z} \tag{37}$$

The total concentration of group V atoms at nucleation and the parameter Γ_l in the liquid−solid distributions depend on the effective vapor composition Z as follows:

$$\chi_A^0 + \chi_B^0 = \sqrt{\frac{\nu_A + \nu_B}{\nu_B^{des}}}\, e^{-\psi_B}(\phi\sqrt{Z} + \sqrt{1 - Z}), \; \Gamma_l = \frac{\Gamma_c}{\phi\sqrt{Z} + \sqrt{1 - Z}} \tag{38}$$

Here, the two important parameters of our theory, φ and Γ_c, are given by

$$\phi = \sqrt{\frac{\nu_B^{des}}{\nu_A^{des}}}\, e^{\psi_B - \psi_A}, \quad \Gamma_c = \phi\sqrt{\Gamma_g} = \sqrt{\frac{\nu_B^{des}}{\nu_A + \nu_B}}\, \frac{e^{-\Delta\mu_{AC}^P + \psi_B - \psi_A - \psi_C}}{\chi_C} \tag{39}$$

Clearly, the parameter φ equals the ratio of the characteristic desorption rates of atoms B over atoms A from liquid with a given percentage of Au. It is noteworthy that $\beta_g = (\varphi\beta_l)^2$ according to the definitions of these parameters. The parameter Γ_c is inversely proportional to the vapor−solid supersaturation for binary AC compound.

Using eqs 37 and 38 in the liquid−solid distribution for $y_0 = l_A^0/(l_A^0 + l_B^0)$, eq 29 is reduced to

$$\phi\sqrt{Z} + \sqrt{1 - Z} = \frac{\phi\sqrt{Z} - \Gamma_c g(x)}{x} \tag{40}$$

This is equivalent to the quadratic equation for $\sqrt{Z}$, which has the solution

$$Z = P^2(x), \quad P(x) = \frac{(1 - x)\phi\Gamma_c g(x)}{x^2 + \phi^2(1 - x)^2} + \frac{x}{\sqrt{x^2 + \phi^2(1 - x)^2}}\sqrt{1 - \frac{\Gamma_c^2 g^2(x)}{x^2 + \phi^2(1 - x)^2}} \tag{41}$$

The stopping size given by eq 27 can be presented as a function of the solid or vapor composition:

$$i_s = l_{tot}\sqrt{\frac{\nu_A + \nu_B}{\nu_B^{des}}}\, e^{-\psi_B}\left[\frac{\phi P(x)}{x} - \Gamma_c\left(1 - 2x\right)e^{\omega(1-x)^2}\right] = l_{tot}\sqrt{\frac{\nu_A + \nu_B}{\nu_B^{des}}}\, e^{-\psi_B}\left[\phi\sqrt{Z} + \sqrt{1 - Z} - \Gamma_c\left(xe^{\omega(1-x)^2} + \beta_l\left(1 - x\right)e^{\omega x^2}\right)\right] \tag{42}$$

No characteristics of atoms A and B in liquid are left in these expressions. Therefore, in VLS $IIIV_xV_{1-x}$ with high desorption rates, the stopping size depends only on the vapor composition and the fraction of Au in liquid.

https://doi.org/10.1021/acs.cgd.4c01338
Cryst. Growth Des. XXXX, XXX, XXX−XXX

Let us now consider the typical values of the control parameters of the vapor–solid distributions Γ_c, Γ_g and φ. With neglect of small corrections containing concentrations of group V atoms χ_A and χ_B, the interaction terms in the chemical potentials entering eqs 31 and 39 are reduced to[52]

$$\psi_C \cong \omega_{CAu}(1-\chi_C)^2 \tag{43}$$

$$\psi_A \cong \omega_{AC}\chi_C + (\omega_{AAu} - \omega_{CAu}\chi_C)(1-\chi_C),$$

$$\psi_B \cong \omega_{BC}\chi_C + (\omega_{BAu} - \omega_{CAu}\chi_C)(1-\chi_C),$$

$$\psi_A - \psi_B \cong (\omega_{AC} - \omega_{BC})\chi_C + (\omega_{AAu} - \omega_{BAu})(1-\chi_C) \tag{44}$$

Here, ω_{ik} denote the temperature-dependent interaction parameters of atoms i and k in liquid. In particular, $\psi_C \cong 0$, $\psi_A \cong \omega_{AC}$, $\psi_B \cong \omega_{BC}$, and $\psi_A - \psi_B \cong \omega_{AC} - \omega_{BC}$ for self-catalyzed VLS growth of at $\chi_C \cong 1$. Hence, the control parameters are expressed through the well-known values of binary chemical potentials $\Delta\mu^p_{AC}$, $\Delta\mu^p_{BC}$ and interaction parameters in liquid, tabulated as functions of temperature in the CALPHAD database.[81,82] The desorption fluxes ν_k^{des} are calculated by equating the chemical potentials of two group V atoms k = A,B in liquid to the chemical potentials of group V dimers in vapor.[75] Using the data of refs 81,82 for the temperature dependences of $\Delta\mu^p_{AC}$ and ω_{ik} and ref 49 for ν_A^{des} and ν_B^{des}, one can plot the parameters Γ_c, Γ_g and φ versus temperature at the given fluxes ν_k of atoms k = A, B and C. In calculation of the desorption fluxes, we take into account that $\nu_k^{des} = 2\sigma_S^{des}\pi R^2 I_{k_2}^{des}$, with $\sigma_S^{des} = 2/[1+\cos(\delta)]$ and $I_{k_2}^{des}$ as the desorption fluxes from unit surface area of the droplet.[49,75] Figure 3 shows the temperature dependences of the

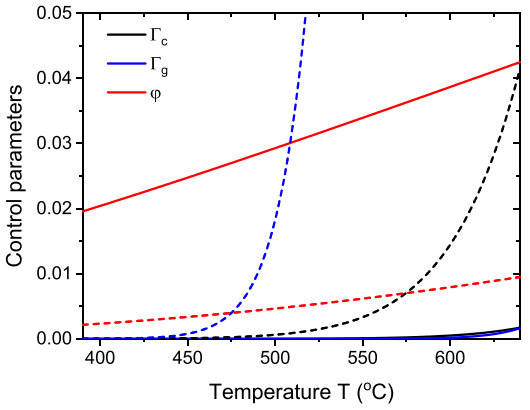

Figure 3. Control parameters of the vapor–solid distribution Γ_c, Γ_g and φ versus temperature for self-catalyzed GaP_xAs_{1-x} (solid lines) and InP_xAs_{1-x} (dashed lines) NWs.

control parameters for self-catalyzed GaP_xAs_{1-x} and InP_xAs_{1-x} NWs. In these calculations, we used the expression

$$\Gamma_c = \frac{1}{\sqrt{F_{53}}}\sqrt{\frac{2\sigma_S^{des} I_{B_2}^{des}}{\sigma_C I_C}}\, e^{-\Delta\mu^p_{AC}+\psi_B-\psi_A-\psi_C} \tag{45}$$

with $F_{53} = (\nu_A+\nu_B)/\nu_C$ as the effective total V/III ratio, assuming $F_{53} = 2$ and $2\sigma_S^{des}/\sigma_C = 0.2$ to account for higher surface diffusivity of group III adatoms.[49,83] The parameter φ was calculated from eq 39 at $\nu_B^{des}/\nu_A^{des} = I_{B_2}^{des}/I_{A_2}^{des}$. The parameter Γ_g was obtained using $\Gamma_c = \phi\sqrt{\Gamma_g}$.

It is seen that both Γ_c and Γ_g are extremely small for both material systems at their typical growth temperatures. For GaP_xAs_{1-x} NWs, Γ_c and Γ_g remain smaller than 0.002 at T < 640 °C. For InP_xAs_{1-x} NWs, Γ_c remains smaller than 0.001 and Γ_g smaller than 0.025 at T < 500 °C. The parameters φ increase almost linearly with T and are also very small in the entire temperature domains, meaning that P atoms desorb much more than As from Ga or In liquid. Figure 4 shows that the presence of

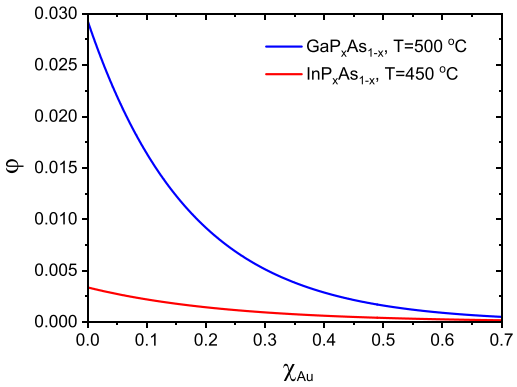

Figure 4. Influence of the Au concentration in the catalyst droplets on the parameter φ for GaP_xAs_{1-x} NWs at 500 °C and InP_xAs_{1-x} NWs at 450 °C.

Au in the catalyst droplet only enhances desorption of P atoms relative to As atoms. This effect persists for any temperature within the growth domains of GaP_xAs_{1-x} and InP_xAs_{1-x} NWs.

The smallness of the parameters Γ_c and Γ_g means that most group V atoms leave a catalyst droplet by desorption from liquid rather than by rejection from the growing solid, at least for $IIIP_xAs_{1-x}$ NWs. At $\Gamma_c \to 0$, the vapor–solid distribution given by eq 41 is simplified to

$$Z = \frac{x^2}{x^2 + \phi^2(1-x)^2} \tag{46}$$

This result for the vapor–solid distribution in regime 2 with high desorption rates has the same form as in ref 49. However, the parameter φ is different, because here we consider the case of $c_l = 1$, while in ref 49 this parameter was modified to $(\varphi c_l)^2$ at $c_l \neq 1$. The desorption-limited vapor–solid distribution given by eq 46 applies before the stopping size i_s. From eq 42, the dependence of the stopping coverage $\theta_s = i_s/i_{ML}$ on the ML composition x and the effective vapor composition Z at $\Gamma_c \to 0$ is reduced to

$$\theta_s = q\frac{\phi}{\sqrt{x^2+\phi^2(1-x)^2}} = [\phi\sqrt{Z} + \sqrt{1-Z}],$$

$$q = \frac{I_{tot}}{i_{ML}}\sqrt{\frac{\nu_A+\nu_B}{\nu_A^{des}}}\, e^{-\psi_B} \tag{47}$$

After the stopping size, no group V adatoms leave the droplet at $\Gamma_g \to 0$. This yields $Z = x$ from eq 31. Therefore, the compositions of the NW MLs, and hence the whole NW, may be different before and after the stopping size in regime 2. This effect is illustrated in Figure 5 for hypothetical system with q = 0.5 and φ = 0.2.

https://doi.org/10.1021/acs.cgd.4c01338
Cryst. Growth Des. XXXX, XXX, XXX−XXX

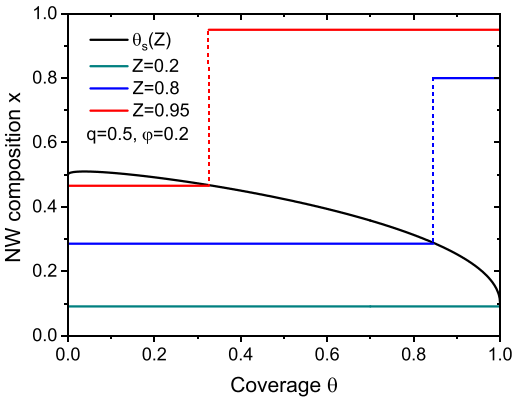

Figure 5. Spatially homogeneous composition of a VLS $IIIV_xV_{1-x}$ NWs at an effective vapor compositions Z of 0.2 without the stopping effect; and spatially inhomogeneous compositions at a higher Z of 0.8 and 0.95, with different compositions of MLs before and after the stopping size (black line).

6. GOVERNING PARAMETER OF THE VAPOR−SOLID DISTRIBUTIONS

In the limit of $\Gamma_g \to 0$ and $\Gamma_c \to 0$, desorption of both group V atoms occurs only in the refill stage in regime 2. The simplified vapor−solid distribution in MLs before the stopping size, or in the whole NW without the stopping effect is given by eq 46. The purely kinetic distribution $Z = x$ applies for any ML size in regime 1, and after the stopping size in regime 2. Regimes 1 and 2 occur at $t_{ML}/t_k \ll 1$ and $t_{ML}/t_k \gg 1$, respectively, corresponding to negligible or high desorption rates in the refill stage. We now assume that $t_{ML} = i_{ML}/v_c$, meaning that the duration of the ML growth cycle is determined by the total influx of group III atoms. Strictly speaking, this approximation corresponds to a time-independent droplet volume and negligible loss of group V atoms by negative diffusion from the droplet onto the NW sidewalls [48−50]. It should be however applicable in the first approximation for our semi-quantitative analysis. We introduce the effective time t_5 required to reach the maximum concentrations of both group V atoms in liquid according to $1/t_5 = 1/t_A + 1/t_B$. Using eq 21 for t_A and t_B, the ratio t_{ML}/t_5 that regulates the occurrence of the VLS growth regimes 1 or 2, can be put as

$$\varepsilon = \frac{t_{ML}}{t_5} = \frac{i_{ML}}{l_{tot}} \frac{\sqrt{\nu_A + \nu_B}}{\nu_c} \left(\sqrt{\nu_A^{des} Z}\, e^{\psi_A} + \sqrt{\nu_B^{des}(1 - Z)}\, e^{\psi_B}\right) \sim \frac{i_{ML}}{l_{tot}} \frac{\sqrt{\nu_A + \nu_B}}{\nu_c} \left(\sqrt{\nu_A^{des}}\, e^{\psi_A} + \sqrt{\nu_B^{des}}\, e^{\psi_B}\right) \quad (48)$$

Generally, this ε depends on the vapor composition, but can approximately be treated composition-independent in the first approximation according to the last expression. Regime 1 corresponds to $\varepsilon \ll 1$ and regime 2 to $\varepsilon \gg 1$.

According to eq 48, the limiting behavior at $\varepsilon \ll 1$ is observed at low desorption rates (low growth temperatures) and small $\nu_A + \nu_B$ compared to ν_c (low V/III flux ratios in vapor). The limiting behavior in the opposite case of $\varepsilon \gg 1$ is observed at high desorption rates (elevated growth temperatures) and large $\nu_A + \nu_B$ compared to ν_c (high V/III flux ratios in vapor). Furthermore, the ML size i_{ML} scales with the NW radius as R^2, while l_{tot} scales as R^3 (and rapidly increases with the droplet contact angle δ). Hence, the ratio i_{ML}/l_{tot} in eq 48 scales as R^{-1}. Assuming that most group V atoms are collected from the droplet surface ($\nu_k \propto R^2$, $\nu_k^{des} \propto R^2$ for $k = A, B$) and that ν_c includes the collection of group III adatoms from a length Λ_3 at the NW top ($\nu_k \propto R^2 + \Lambda_3 R$), we obtain $\varepsilon \propto (R + \Lambda_3)^{-1}$. Hence, the parameter ε is size-dependent and decreases with the NW radius. This governing parameter is more complex than the effective V/III flux ratio $F_{53} = (\nu_A + \nu_B)/\nu_C$ considered in the stationary models of refs 47−50 and depends differently on temperature, material fluxes and NW geometry.

Our model gives the analytic vapor−solid distributions in the two limiting cases of $\varepsilon \ll 1$ and $\varepsilon \gg 1$. The simple interpolation formula that yields the two limiting behaviors and approximates the vapor−solid distribution at any ε is given by

$$Z = \frac{x + \varepsilon F(x)}{1 + \varepsilon},$$

$$F(x) = \frac{x^2}{x^2 + \phi^2(1 - x)^2} \text{ at } 0 \le \theta \le \theta_s(x),$$

$$Z = x \text{ for any } \varepsilon \text{ at } \theta > \theta_s(x) \quad (49)$$

This distribution connects the solid composition x with the effective vapor composition Z. As discussed above, the fraction of atoms A in vapor z may be different from Z due to several factors including different adsorption coefficients of atoms A and B on the droplet surface,[27,37,39] different diffusivities of adatoms A and B on the NW sidewalls,[76,77] and different re-emission of atoms A and B.[75] These effects are described by the coefficient c_g in eq 2. Using eq 2 in eq 49, the fraction of atoms A in vapor is obtained in the form

$$z = \frac{x + \varepsilon F(x)}{x + c_g(1 - x) + \varepsilon[F(x) + c_g(1 - F(x))]} \text{ at } 0 \le \theta \le \theta_s(x),$$

$$z = \frac{x}{x + c_g(1 - x)} \text{ for any } \varepsilon \text{ at } \theta > \theta_s(x) \quad (50)$$

According to our analysis, this simplified vapor−solid distribution applies to VLS systems with $\Gamma_c \ll 1$ and $\Gamma_g \ll 1$, that is, when most group V atoms desorb from the droplet surface in the refill stage. This is not guaranteed in the general

Table 1. Description of the Parameters in the Vapor−solid Distribution

parameter	role in NW composition	temperature dependence	V/III ratio dependence	radius dependence
desorption-related parameter φ	enhances fraction of more stable group V atoms that desorb less from liquid; applies before the stopping size	increases with T for $IIIP_xAs_{1-x}$ NWs	independent	independent
kinetic parameter c_g	enhances fraction of group V atoms with larger adsorption or surface diffusion; fully controls the composition after the stopping size.	increases with T for $IIIP_xAs_{1-x}$ NWs according to the fits in Figure 8	unknown	unknown
governing parameter ε	regulates the weights of the desorption-limited and kinetic vapor−solid distributions; applies before the stopping size.	increases with T	increases with V/III ratio	decreases with R

https://doi.org/10.1021/acs.cgd.4c01338
Cryst. Growth Des. XXXX, XXX, XXX−XXX

case, and should be checked for any particular $IIIV_xV_{1-x}$ system for a given set of growth conditions. The general solutions given by eqs 31 and 41 with larger Γ_c and Γ_g include interactions in liquid in the x−dependent rejected fluxes of AC and BC pairs. Equation 41 before the stopping size also includes the affinity parameter β_l in liquid. We suspect that $\varphi\beta_l \cong 1$, that is, a group V atom that desorbs more from liquid ($\varphi < 1$ or $\varphi \ll 1$) has larger affinity ($\beta_l > 1$ or $\beta_l \gg 1$). This is definitely true for P atoms in Ga−Au and In−Au liquids during the VLS growth of $IIIP_xAs_{1-x}$ NWs.[52,53] Another important assumption is the equal diffusivities of atoms A and B in liquid, corresponding to $c_l = 1$. Different diffusion transport of dissimilar atoms in liquid modifies the constant φ.49 Even more importantly, it leads to spatially inhomogeneous compositions in the "core" and "shell" regions growing before and after the stopping size. Equation 50 contains three parameters φ, c_g and ε. Table 1 summarizes the physical meaning, role in the NW composition and dependence of these parameters on the growth temperature, V/III flux ratio in vapor and NW radius.

Figure 6 shows the vapor−solid distributions of self-catalyzed GaP_xAs_{1-x} NWs at 630 °C, with $\varphi = 0.0415$ according to Figure 3. The kinetic parameter $c_g = 2.97$ is taken from ref 37, where the measured vapor−solid distributions of GaP_xAs_{1-x} NWs at 630 °C were well-fitted by the LM formula with this c_g. In this example, the desorption-limited behavior at large $\varepsilon \gg 1$ before the stopping size favors the incorporation of GaAs pairs relative to GaP. Conversely, a faster transport of P atoms from vapor to liquid at $c_g > 1$ favors the incorporation of GaP pairs relative to GaAs. As a result, the curves before the stopping size transition from the desorption-limited regime with low GaP fractions in solid at large ε to the kinetic LM shape with high GaP fractions in solid. This picture applies to the whole NW if the stopping size is larger than unity for all x. If, on the contrary, the stopping size is much smaller than unity for all x, the vapor−solid distribution is given by the LM shape for almost all regions of the NW. The LM shapes of the measured vapor−solid distributions of most VLS GaP_xAs_{1-x}[35,37,39,41] and InP_xAs_{1-x}[29] NWs (or NW sections) can thus be explained by (i) the effective absence of desorption of both group V atoms in any stage of ML growth, (ii) small stopping size, after which the NW composition is determined only by the material transport into the droplet, or (iii) faster transfer of P atoms through liquid at $c_l > 1$.49 The last explanation is ruled out in our model with $c_l = 1$. The first two factors will be considered in detail in the next section.

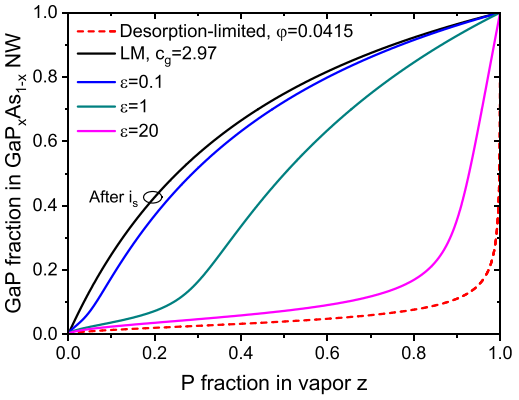

Figure 6. Vapor−solid distributions of self-catalyzed GaP_xAs_{1-x} NWs at 630 °C, obtained from eq 50 at $\varphi = 0.0415$, $c_g = 2.97$ and different ε shown in the legend. After the stopping size, the distribution is reduced to the LM shape (black line labeled "after i_s"). Dashed line shows the desorption-limited curve at $\varepsilon \to \infty$.

It should be emphasized that different compositional trends in MLs before and after the stopping size should hold only for WZ $IIIV_xV_{1-x}$ NWs. As mentioned above, most ZB III−V NWs show the oscillating truncated geometry of the liquid−solid interface.[56,57,70] In ZB NWs, the truncation provides additional material to complete the ML after the stopping size. Therefore, the composition of the MLs grown after the stopping size should be the same as the composition of the truncated region underneath. In the simplest approximation, our results before the stopping size describe the composition of the whole ML in ZB NWs, where the slow growth stage from vapor is absent. This approximation neglects, however, a lot of important details that regard the growth kinetics of the truncated interfaces in ternary NWs, and should be refined in the future.

7. THEORY AND EXPERIMENT

Figure 7 shows the vapor−solid distributions of Au-catalyzed $InSb_xAs_{1-x}$ NWs.[20] These NWs were grown by metal−organic vapor phase epitaxy (MOVPE) on InAs(111)B substrates at 450 °C from TMIn, TMSb and AsH_3 precursors, with 50 nm diameter colloidal Au nanoparticles as the VLS growth seeds. The total V/III flux ratio in vapor was set to 15, 27, and 56 by varying group V fluxes at a constant flux of TMIn. The crystal phase of the NWs was pure ZB, without stacking faults. The compositional data were originally fitted by the model of Biefeld for epi-layers,[44] with largely reduced effective V/III flux ratios that accounted for surface diffusion of In adatoms from the surrounding surfaces.[20] Later on, the same data were fitted by a combination of the kinetic ($z = x$) and equilibrium vapor−solid distributions, whose weights were regulated by the effective V/III ratio F_{53}.[48,50] The fits of ref 48 are shown by dashed lines in the figure. Solid lines show the equally good fits obtained from eq 50 before the stopping size (due to pure ZB crystal phase of the NWs) at a fixed $\varphi = 0.11$, $c_g = 1$ and different ε. The fitting values of ε increase with the total group V flux $\nu_A + \nu_B$ in vapor according to eq 48. Of course, increasing $\nu_A + \nu_B$ at a fixed ν_C is equivalent to increasing the total V/III flux ratio in vapor. As regards the fitting value of φ of 0.11, it corresponds to strong suppression of Sb incorporation in the desorption-limited regime. The concentration of Au in the NWs is unknown, and

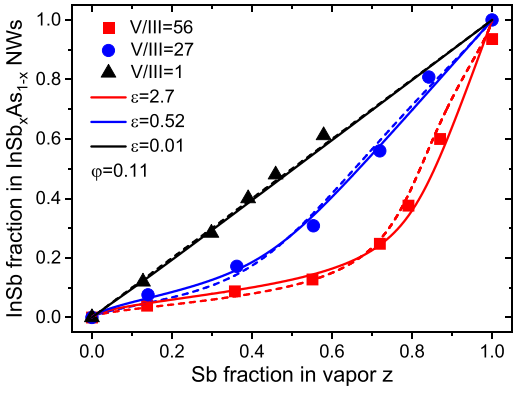

Figure 7. Vapor−solid distributions of Au-catalyzed $InSb_xAs_{1-x}$ NWs at 450 °C, obtained under different total V/III flux ratios in vapor shown in the legend (symbols),[20] fitted by the model of ref 48 (dashed lines) and by eq 50 before the stopping size at a fixed φ of 0.11, $c_g = 1$ and different ε shown in the legend.

https://doi.org/10.1021/acs.cgd.4c01338
Cryst. Growth Des. XXXX, XXX, XXX−XXX

may change depending on the V/III flux ratio, so the constant φ for the whole data set should be considered as a fitting parameter that determines the composition in the close-to-equilibrium regime under group V rich conditions.[44,48,50] The fitting value of $c_g = 1$ yields the linear vapor−solid distribution $z = x$ in the kinetic regime under a balanced V/III ratio.

Figure 8 shows a compilation of the vapor−solid distributions of $IIIP_xAs_{1-x}$ NWs obtained in different works. InP_xAs_{1-x} NW

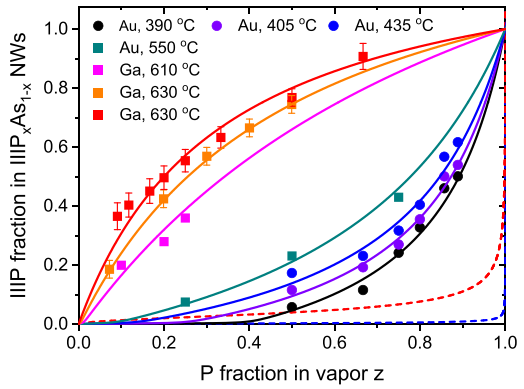

Figure 8. Vapor−solid distributions of InP_xAs_{1-x} NW sections on InAs stems obtained by Au-catalyzed CBE at 390 °C, 405 and 435 °C in ref 29 (circles), GaP_xAs_{1-x} NWs obtained by Au-catalyzed aerotaxy at 550 °C in ref 39, Ga-catalyzed MBE at 610 °C in ref 35 and 630 °C in ref 37, and GaP_xAs_{1-x} quantum discs in GaP NWs obtained by Ga-catalyzed MBE at 630 °C in ref 41 (squares). Solid lines are the fits by eq 50 with the parameters given in Table 2. Dashed lines show the desorption-limited distributions of InP_xAs_{1-x} NWs at 435 °C and GaP_xAs_{1-x} NWs at 630 °C, which are obviously far from the experimental data for both material systems.

sections of ref 29 were grown by chemical beam epitaxy (CBE) on InAs(111)B substrates at three different temperatures of 390 °C, 405 and 435 °C. The growth started with InAs NW stems and continued with InP_xAs_{1-x} sections having an average radius of 30 nm and pure WZ crystal phase The total V/III flux ratio in vapor during growth of InP_xAs_{1-x} sections was in the range from 30 to 45. GaP_xAs_{1-x} NWs of ref 39 were grown by Au-catalyzed MOVPE using the substrate-free aerotaxy at 550 °C, under a balanced total V/III flux ratio in vapor ranging from 0.82 to 1.64. These NWs formed in the ZB phase, with low density of stacking faults. Other GaP_xAs_{1-x} NWs were grown by Ga-catalyzed MBE on Si(111) substrates. GaP_xAs_{1-x} NWs of ref 35 were grown at 610 °C under the total V/III flux ratios ranging from 10 to 12. These NWs had an average radius of 70 nm and a mixed ZB/WZ crystal structure. GaP_xAs_{1-x} NWs of ref 37 were grown at 630 °C under the total V/III flux ratios around 50. These NWs had an average radius of 30 nm and predominantly ZB crystal phase. GaP_xAs_{1-x} quantum discs in GaP NWs of ref 41 were grown at 630 °C under the total V/III flux ratios ranging from 16 (for low As/P ratios in vapor) to 32 (for high As/P ratios). The average radius of GaP_xAs_{1-x} sections was 110 nm, with predominantly WZ crystal phase (in contrast to the ZB phase of binary GaP NWs). The data in the figure correspond to the stationary compositions in the interfacial profiles across GaP/GaP_xAs_{1-x}/GaP NW heterostructures.

These $IIIP_xAs_{1-x}$ NWs (or NW sections) were obtained under very different conditions and on different substrates, using either Au−III or pure Ga droplets. The resulting radii and crystal phases were also very different. The compositional data were fitted by different models in the original works[29,35,37,39,41] and in refs 48,49. Considering the whole data set in Figure 8, we can see two clear trends. First, the measured IIIP fraction in $IIIP_xAs_{1-x}$ NWs systematically increases with temperature. Second, it is systematically higher in NWs grown without Au. The desorption-limited vapor−solid distributions given by eq 50 before the stopping size and at $c_g = 1$ largely underestimate the IIIP content in NWs. The best fits are obtained with the parameters summarized in Table 2. Within our model,

Table 2. Fitting Parameters of the Vapor−Solid Distributions in Figure 8

material system, growth temperature	φ	c_g	ε
Au-catalyzed InP_xAs_{1-x}/InP NWs, 390 °C [29]	0.0215	0.143	0.09
Au-catalyzed InP_xAs_{1-x}/InP NWs, 405 °C [29]	0.0242	0.16	0.05
Au-catalyzed InP_xAs_{1-x}/InP NWs, 435 °C [29]	0.0303	0.19	0.025
Au-catalyzed GaP_xAs_{1-x} NWs, 550 °C [39]	0.0339	0.3	0.025
Ga-catalyzed GaP_xAs_{1-x} NWs, 610 °C [35]	0.0396	2.0	0.02
Ga-catalyzed GaP_xAs_{1-x} NWs, 630 °C [37]	0.0415	2.97	0.01
Ga-catalyzed GaP/GaP_xAs_{1-x}/GaP NWs, 630 °C [41]	0.0415	4.0	0

desorption of group V elements from liquid appears low in all cases, which corresponds to small ε decreasing with temperature from 0.09 for InP_xAs_{1-x} NWs at 390 °C to 0 for GaP_xAs_{1-x} NWs at 630 ° C. The fitting values of c_g increase with temperature from 0.143 for InP_xAs_{1-x} NWs at 390 °C to a high value ranging from 3 to 4 for GaP_xAs_{1-x} NWs at 630 ° C. Consequently, all vapor−solid distributions are well approximated by the purely kinetic LM shapes, with $c_g \neq 1$. This observation was made in the original works[29,37] and later in ref 48. From our eq 50, this property strongly suggests that (i) most P and As atoms are scattered from the droplet surface without entering the liquid phase, and (ii) this process favors incorporation of As atoms at low temperatures ≤550 °C and P atoms at high temperatures ≥610 °C. The preferred incorporation of P atoms may be enhanced by the absence of Au in liquid. The effective absence of desorption may also be enhanced by a small stopping size in WZ NWs.[29,41] Another possible explanation of the enhanced incorporation of P atoms, recently suggested in ref 49, is based on the assumption of a faster transport of P atoms through liquid. This required introduction of the temperature-dependent factor c_l that strongly increased with temperature.[49] Overall, our analysis shows that more investigations are required to fully understand the growth kinetics and composition of $IIIV_xV_{1-x}$ MLs in NWs. Such studies should carefully reveal the possible spatial inhomogeneity in the NW compositions across their axis and, most importantly, in situ TEM monitoring of the NW growth. Unfortunately, no in situ TEM data on III−V ternary NWs are available to this end.

8. CONCLUSIONS AND OUTLOOK

In summary, we have presented the very first study of the growth kinetics of III−V ternary MLs and the corresponding composition of III−V ternary NWs taking into account the effect of group V depletion in quasi-instantaneous ML growth. The study was restricted to the case of WZ NWs based on group V intermix and, very importantly, identical diffusion transport rates of both group V atoms in liquid ($c_l = 1$). The critical size of ternary nucleus was assumed negligible. The main findings can be put as follows. The liquid−solid distribution of $IIIV_xV_{1-x}$ NWs is kinetic at nucleation, but transitions to the equilibrium shape at the stopping size. The kinetic shape of the liquid−solid

https://doi.org/10.1021/acs.cgd.4c01338
Cryst. Growth Des. XXXX, XXX, XXX−XXX

distribution at any ML size approximately applies only to NWs without the stopping effect. Furthermore, the only liquid−solid distribution that makes physical sense in the one at nucleation. Modeling of the vapor−solid distribution with the technologically controlled parameters (temperature and material fluxes) requires a relationship between the liquid composition at nucleation and the vapor composition. This complex problem was solved in the two limiting cases, either in the effective absence of desorption or at high desorption rates of group V atoms from a catalyst droplet. The intermediate regimes were described using the interpolation formula with the governing parameter ε. It was found that the composition-dependent terms in the vapor−solid distribution appear almost negligible under the typical growth conditions of GaP_xAs_{1-x} and InP_xAs_{1-x} NWs regardless of their catalyst. Then, the vapor−solid distribution is reduced to a simple combination of the purely kinetic and desorption-limited curves, whose weights are regulated by the parameter ε. The model shows that, in the regimes with high desorption, most group V atoms desorb from the droplet in the refill stage. Desorption is absent in the fast ML growth stage before the stopping size, and almost negligible in the slow ML growth stage after the stopping size. This property naturally leads to spatial inhomogeneity in the NW composition, which should be carefully checked in the experimental studies. The model provides excellent fits to the compositional data on $InSb_xAs_{1-x}$, InP_xAs_{1-x} and GaP_xAs_{1-x} NWs. The data analysis for $IIIP_xAs_{1-x}$ NWs leads to the LM-type vapor−solid distributions in the wide range of growth conditions. This observation calls for further studies.

The obtained results may be used in the first approximation for the analysis and prediction of the compositional trends in different material systems and epitaxy techniques. However, the developed theory should be refined in several respects. Introduction of different transport rates of group V atoms through liquid ($c_l \neq 1$) will significantly complicate the analysis and lead to a more spatially inhomogeneous compositions of ternary MLs. Precise in situ measurements of the fast growth stage of ternary MLs are absolutely required to access the characteristics of the diffusion transport of different atoms in liquid droplets, which largely influence the ML composition. The stationary liquid−solid distributions of III−V ternary NWs based on group III intermix were shown to be close-to-equilibrium, because the liquid−solid growth always proceeds under group III rich conditions.[47] However, this stationary picture may be modified by the depletion of group V atoms, and affect the measured vapor−solid distributions of such NWs. It will be interesting to study in detail the growth kinetics of single ternary MLs and its influence on the composition of NWs obtained by non-VLS techniques such as self-induced catalyst-free growth[84−86] or liquid phase epitaxy with an overpressure of group V species.[87] Spontaneous formation of core−shell structures in catalyst-free III-nitride ternary NWs was modeled using DFT and mesoscopic phase field methods.[84,85] It was recently suggested that spontaneous core−shell structures in $In_xGa_{1-x}N$ NWs are due to the periodically changing environment for rapid growth of single ternary MLs in the absence of refill.[86] This effect is also caused by the depletion of group V atoms from the growth reservoir, and may be general for VLS and non-VLS NWs based on group III intermix.[86,88] Finally, more investigations are required to precisely relate the initial liquid composition at nucleation to the vapor fluxes of different elements. This may require additional considerations of nucleation of III−V ternary nuclei and nonzero critical size. It was previously shown that the liquid−solid distribution of critical ternary island is equilibrium.[52,53] The equilibrium shape of the critical island at nucleation may be inherited, at least for some time, in a later stage of ML growth, but this effect is totally ignored in the kinetic approach. We plan to study these interesting problems in the forthcoming works.

AUTHOR INFORMATION

Corresponding Author

Vladimir G. Dubrovskii − *Faculty of Physics, St. Petersburg State University, St. Petersburg 199034, Russia;* orcid.org/0000-0003-2088-7158; Email: dubrovskii@mail.ioffe.ru

Complete contact information is available at: https://pubs.acs.org/10.1021/acs.cgd.4c01338

Funding

This research was supported by the research grant of St. Petersburg State University (ID 95440344).

Notes

The author has declared that no competing financial or nonfinancial interests existed at the time of publication. The author declares no competing financial interest.

REFERENCES

(1) Ning, C.-Z.; Dou, L.; Yang, P. Bandgap engineering in semiconductor alloy nanomaterials with widely tunable compositions. *Nat. Rev. Mater.* **2017**, *2*, 17070.

(2) McIntyre, P. C.; Fontcuberta i Morral, A. Semiconductor nanowires: to grow or not to grow? *Mater. Today Nano* **2020**, *9*, No. 100058.

(3) Boras, G.; Yu, X.; Liu, H. III−V ternary nanowires on Si substrates: growth, characterization and device applications. *J. Semicond.* **2019**, *40*, No. 101301.

(4) Johansson, J.; Dick, K. A. Recent advances in semiconductor nanowire heterostructures. *CrystEngComm* **2011**, *13*, 7175.

(5) Hyun, J. K.; Zhang, S.; Lauhon, L. J. Nanowire heterostructures. *Annu. Rev. Mater. Research* **2013**, *43*, 451.

(6) Glas, F. Critical dimensions for the plastic relaxation of strained axial heterostructures in free-standing nanowires. *Phys. Rev. B* **2006**, *74*, No. 121302(R).

(7) Chuang, L. C.; Moewe, M.; Chase, C.; Kobayashi, N. P.; Chang-Hasnain, C.; Crankshaw, S. Critical diameters for III-V nanowires grown on lattice-mismatched substrates. *Appl. Phys. Lett.* **2007**, *90*, No. 043115.

(8) Ren, D.; Ahtapodov, L.; Nilsen, J. S.; Yang, J.; Gustafsson, A.; Huh, J.; Conibeer, G. J.; Van Helvoort, A. T.; Fimland, B. O.; Weman, H. Single-mode near-infrared lasing in a GaAsSb-based nanowire superlattice at room temperature. *Nano Lett.* **2018**, *18*, 2304.

(9) Haffouz, S.; Zeuner, K. D.; Dalacu, D.; Poole, P. J.; Lapointe, J.; Poitras, D.; Mnaymneh, K.; Wu, X.; Couillard, M.; Korkusinski, M.; Schöll, E.; Jöns, K. D.; Zwiller, V.; Williams, R. L. Bright single InAsP quantum dots at telecom wavelengths in position-controlled InP nanowires: the role of the photonic waveguide. *Nano Lett.* **2018**, *18*, 3047.

(10) Singh, R.; Bester, G. Nanowire quantum dots as an ideal source of entangled photon pairs. *Phys. Rev. Lett.* **2009**, *103*, No. 063601.

(11) Leandro, L.; Gunnarsson, C. P.; Reznik, R.; Jöns, K. D.; Shtrom, I.; Khrebtov, A.; Kasama, T.; Zwiller, V.; Cirlin, G.; Akopian, N. Nanowire quantum dots tuned to atomic resonances. *Nano Lett.* **2018**, *18*, 7217.

(12) Dalacu, D.; Poole, P. J.; Williams, R. L. Nanowire-based sources of non-classical light. *Nanotechnology* **2019**, *30*, No. 232001.

(13) Wagner, R. S.; Ellis, W. C. Vapor-liquid-solid mechanism of single crystal growth. *Appl. Phys. Lett.* **1964**, *4*, 89.

(14) Colombo, C.; Spirkoska, D.; Frimmer, M.; Abstreiter, G.; Fontcuberta i Morral, A. Ga-assisted catalyst-free growth mechanism of

GaAs nanowires by molecular beam epitaxy. *Phys. Rev. B* **2008**, *77*, No. 155326.
(15) Paladugu, M.; Zou, J.; Guo, Y.-N.; Zhang, X.; Kim, Y.; Joyce, H. J.; Gao, Q.; Tan, H. H.; Jagadish, C. Nature of heterointerfaces in GaAs/InAs and InAs/GaAs axial nanowire heterostructures. *Appl. Phys. Lett.* **2008**, *93*, No. 101911.
(16) Heiß, M.; Gustafsson, A.; Conesa-Boj, S.; Peiró, F.; Morante, J. R.; Abstreiter, G.; Arbiol, J. G.; Samuelson, L.; Fontcuberta i Morral, A. Catalyst-free nanowires with axial $In_xGa_{1-x}As$/GaAs heterostructures. *Nanotechnology* **2009**, *20*, No. 075603.
(17) Priante, G.; Glas, F.; Patriarche, G.; Pantzas, K.; Oehler, F.; Harmand, J. C. Sharpening the interfaces of axial heterostructures in self-catalyzed AlGaAs nanowires: experiment and theory. *Nano Lett.* **2016**, *16*, 1917.
(18) Dick, K. A.; Bolinsson, J.; Borg, B. M.; Johansson, J. Controlling the abruptness of axial heterojunctions in III−V nanowires: beyond the reservoir effect. *Nano Lett.* **2012**, *12*, 3200.
(19) Sjokvist, R.; Jacobsson, D.; Tornberg, M.; Wallenberg, R.; Leshchenko, E. D.; Johansson, J.; Dick, K. A. Compositional correlation between the nanoparticle and the growing Au-assisted $In_xGa_{1-x}As$ nanowire. *J. Phys. Chem. Lett.* **2021**, *12*, 7590.
(20) Borg, B. M.; Dick, K. A.; Eymery, J.; Wernersson, L.-E. Enhanced Sb incorporation in InAsSb nanowires grown by metalorganic vapor phase epitaxy. *Appl. Phys. Lett.* **2011**, *98*, No. 113104.
(21) Namazi, L.; Ghalamestani, S. G.; Lehmann, S.; Zamani, R. R.; Dick, K. A. Direct nucleation, morphology and compositional tuning of $InAs_{1-x}Sb_x$ nanowires on InAs (111)B substrates. *Nanotechnology* **2017**, *28*, No. 165601.
(22) Zhuang, Q. D.; Alradhi, H.; Jin, Z. M.; Chen, X. R.; Shao, J.; Chen, X.; Sanchez, A. M.; Cao, Y. C.; Liu, J. Y.; Yates, P.; Durose, K.; Jin, C. J. Optically-efficient InAsSb nanowires for silicon-based mid-wavelength infrared optoelectronics. *Nanotechnology* **2017**, *28*, No. 105710.
(23) Wen, L.; Pan, D.; Liu, L.; Tong, S.; Zhuo, R.; Zhao, J. Large-composition-range pure-phase homogeneous $InAs_{1-x}Sb_x$ nanowires. *J. Phys. Chem. Lett.* **2022**, *13*, 598.
(24) Yuan, X.; Caroff, P.; Wong-Leung, J.; Tan, H. H.; Jagadish, C. Controlling the morphology, composition and crystal structure in gold-seeded $GaAs_{1-x}Sb_x$ nanowires. *Nanoscale* **2015**, *7*, 4995.
(25) Dheeraj, D. L.; Patriarche, G.; Zhou, H.; Harmand, J. C.; Weman, H.; Fimland, B. O. Growth and structural characterization of GaAs/GaAsSb axial heterostructured nanowires. *J. Cryst. Growth* **2009**, *311*, 1847.
(26) Plissard, S.; Dick, K. A.; Wallart, X.; Caroff, P. Gold-free GaAs/GaAsSb heterostructure nanowires grown on silicon. *Appl. Phys. Lett.* **2010**, *96*, No. 121901.
(27) Ren, D.; Ahtapodov, L.; Nilsen, J. S.; Yang, J.; Gustafsson, A.; Huh, J.; Conibeer, G. J.; Van Helvoort, A. T.; Fimland, B. O.; Weman, H. Single-mode near-infrared lasing in a GaAsSb-based nanowire superlattice at room temperature. *Nano Lett.* **2018**, *18*, 2304.
(28) Ek, M.; Borg, B. M.; Johansson, J.; Dick, K. A. Diameter limitation in growth of III-Sb-containing nanowire heterostructures. *ACS Nano* **2013**, *7*, 3668.
(29) Persson, A. I.; Bjork, M. T.; Jeppesen, S.; Wagner, J. B.; Wallenberg, L. R.; Samuelson, L. $InAs_{1-x}P_x$ nanowires for device engineering. *Nano Lett.* **2006**, *6*, 403.
(30) Tchernycheva, M.; Cirlin, G. E.; Patriarche, G.; Travers, L.; Zwiller, V.; Perinetti, U.; Harmand, J. C. Growth and characterization of InP nanowires with InAsP insertions. *Nano Lett.* **2007**, *7*, 1500.
(31) Mandl, B.; Keplinger, M.; Messing, M. E.; Kriegner, D.; Wallenberg, R.; Samuelson, L.; Bauer, G.; Stangl, J.; Holy, V.; Deppert, K. Self-seeded axio-radial InAs-$InAs_{1-x}P_x$ nanowire heterostructures beyond "common" VLS growth. *Nano Lett.* **2018**, *18*, 144.
(32) Tateno, K.; Zhang, G.; Gotoh, H.; Sogawa, T. VLS growth of alternating InAsP/InP heterostructure nanowires for multiple-quantum-dot structures. *Nano Lett.* **2012**, *12*, 2888.
(33) Zannier, V.; Rossi, F.; Ercolani, D.; Sorba, L. Growth dynamics of InAs/InP nanowire heterostructures by Au-assisted chemical beam epitaxy. *Nanotechnology* **2019**, *30*, No. 094003.
(34) Bucci, G.; Zannier, V.; Rossi, F.; Musiał, A.; Boniecki, J.; Sęk, G.; Sorba, L. Zincblende $InAs_xP_{1-x}$/InP quantum dot nanowires for telecom wavelength emission. *ACS Appl. Mater. Interfaces* **2024**, *16*, 26491.
(35) Himwas, C.; Collin, S.; Rale, P.; Chauvin, N.; Patriarche, G.; Oehler, F.; Julien, F. H.; Travers, L.; Harmand, J. C.; Tchernycheva, M. In situ passivation of GaAsP nanowires. *Nanotechnology* **2017**, *28*, No. 495707.
(36) Zhang, Y.; Sanchez, A. M.; Sun, Y.; Wu, J.; Aagesen, M.; Huo, S.; Kim, D.; Jurczak, P.; Xu, X.; Liu, H. Influence of droplet size on the growth of self-catalyzed ternary GaAsP nanowires. *Nano Lett.* **2016**, *16*, 1237.
(37) Zhang, Y.; Aagesen, M.; Holm, J. V.; Jørgensen, H. I.; Wu, J.; Liu, H. Self-catalyzed GaAsP nanowires grown on silicon substrates by solid-source molecular beam epitaxy. *Nano Lett.* **2013**, *13*, 3897.
(38) Zhang, Y.; Velichko, A. V.; Fonseka, H. A.; Parkinson, P.; Gott, J. A.; Davis, G.; Aagesen, M.; Sanchez, A. M.; Mowbray, D.; Liu, H. Defect-free axially-stacked GaAs/GaAsP nanowire quantum dots with strong carrier confinement. *Nano Lett.* **2021**, *21*, 5722.
(39) Metaferia, W.; Persson, A. R.; Mergenthaler, K.; Yang, F.; Zhang, W.; Yartsev, A.; Wallenberg, R.; Pistol, M. E.; Deppert, K.; Samuelson, L.; Magnusson, M. H. GaAsP nanowires grown by aerotaxy. *Nano Lett.* **2016**, *16*, 5701.
(40) Priante, G.; Patriarche, G.; Oehler, F.; Glas, F.; Harmand, J. C. Abrupt GaP/GaAs interfaces in self-catalyzed nanowires. *Nano Lett.* **2015**, *15*, 6036.
(41) Bolshakov, A. D.; Fedorov, V. V.; Sibirev, N. V.; Fetisova, M. V.; Moiseev, E. I.; Kryzhanovskaya, N. V.; Koval, O. Y.; Ubyivovk, E. V.; Mozharov, A. M.; Cirlin, G. E.; Mukhin, I. S. Growth and characterization of GaP/GaPAs nanowire heterostructures with controllable composition. *Phys. Stat. Sol. RRL* **2019**, *13*, No. 1900350.
(42) Boulanger, J. P.; LaPierre, R. R. Unveiling transient GaAs/GaP nanowire growth behavior using group V oscillations. *Cryst. Growth* **2014**, *388*, 116.
(43) McLean, D. *Grain boundaries in metals*; Oxford University Press:New York, 1957.
(44) Biefeld, R. M. The preparation of InSb and $InAs_{1-x}Sb_x$ by metalorganic chemical vapor deposition. *J. Cryst. Growth* **1986**, *75*, 255.
(45) Ghasemi, M.; Leshchenko, E. D.; Johansson, J. Assembling your nanowire: an overview of composition tuning in ternary III−V nanowires. *Nanotechnology* **2021**, *32*, No. 072001.
(46) Leshchenko, E. D.; Dubrovskii, V. G. An overview of modeling approaches for compositional control in III−V ternary nan-owires. *Nanomaterials* **2023**, *13*, 1659.
(47) Dubrovskii, V. G. Liquid-solid and vapor-solid distributions of vapor-liquid-solid III-V ternary nanowires. *Phys. Rev. Materials* **2023**, *7*, No. 096001.
(48) Dubrovskii, V. G. Circumventing the uncertainties of the liquid phase in the compositional control of VLS III−V ternary nanowires based on group V intermix. *Nanomaterials* **2024**, *14*, 207.
(49) Dubrovskii, V. G.; Leshchenko, E. D. Interplay of kinetic and thermodynamic factors in the stationary composition of vapor-liquid-solid IIIVxV1-x nanowires. *Nanomaterials* **2024**, *14*, 1333.
(50) Dubrovskii, V. G.; Leshchenko, E. D. Composition of III-V ternary materials under arbitrary material fluxes: the general approach unifying kinetics and thermodynamics. *Phys. Rev. Materials* **2023**, *7*, No. 074603.
(51) Glas, F. Comparison of modeling strategies for the growth of heterostructures in III−V nanowires. *Cryst. Growth Des.* **2017**, *17*, 4785.
(52) Dubrovskii, V. G.; Koryakin, A. A.; Sibirev, N. V. Understanding the composition of ternary III-V nanowires and axial nanowire heterostructures in nucleation-limited regime. *Mater. Design* **2017**, *132*, 400.
(53) Leshchenko, E. D.; Ghasemi, M.; Dubrovskii, V. G.; Johansson, J. Nucleation-limited composition of ternary III−V nanowires forming from quaternary gold based liquid alloys. *CrystEngComm* **2018**, *20*, 1649.
(54) Johansson, J.; Ghasemi, M. Kinetically limited composition of ternary III-V nanowires. *Phys. Rev. Mater.* **2017**, *1*, No. 040401(R).

https://doi.org/10.1021/acs.cgd.4c01338
Cryst. Growth Des. XXXX, XXX, XXX−XXX

(55) Glas, F.; Harmand, J. C.; Patriarche, G. Nucleation antibunching in catalyst-assisted nanowire growth. *Phys. Rev. Lett.* **2010**, *104*, No. 135501.
(56) Wen, C.-Y.; Tersoff, J.; Hillerich, K.; Reuter, M. C.; Park, J. H.; Kodambaka, S.; Stach, E. A.; Ross, F. M. Periodically changing morphology of the growth interface in Si, Ge, and GaP nanowires. *Phys. Rev. Lett.* **2011**, *107*, No. 025503.
(57) Jacobsson, D.; Panciera, F.; Tersoff, J.; Reuter, M. C.; Lehmann, S.; Hofmann, S.; Dick, K. A.; Ross, F. M. Interface dynamics and crystal phase switching in GaAs nanowires. *Nature* **2016**, *531*, 317.
(58) Oh, S. H.; Chisholm, M. F.; Kauffmann, Y.; Kaplan, W. D.; Luo, W.; Rühle, M.; Scheu, C. Oscillatory mass transport in vapor-liquid-solid growth of sapphire nanowires. *Science* **2010**, *330*, 489.
(59) Gamalski, A. D.; Ducati, C.; Hofmann, S. Cyclic supersaturation and triple phase boundary dynamics in germanium nanowire growth. *J. Phys. Chem. C* **2011**, *115*, 4413.
(60) Glas, F. Statistics of sub-Poissonian nucleation in a nanophase. *Phys. Rev. B* **2014**, *90*, No. 125406.
(61) Glas, F.; Dubrovskii, V. G. Self-narrowing of size distributions of nanostructures by nucleation antibunching. *Phys. Rev. Materials* **2017**, *1*, No. 036003.
(62) Koivusalo, E.; Hakkarainen, T.; Guina, M. D.; Dubrovskii, V. G. Sub-Poissonian narrowing of length distributions realized in Ga-catalyzed GaAs nanowires. *Nano Lett.* **2017**, *17*, 5350.
(63) Dubrovskii, V. G. Refinement of nucleation theory for vapor-liquid-solid nanowires. *Cryst. Growth Des.* **2017**, *17*, 2589.
(64) Rusanov, A. I. The thermodynamics of processes of new-phase formation. *Russ. Chem. Rev.* **1964**, *33*, 385.
(65) Reguera, D.; Bowles, R. K.; Djikaev, Y.; Reiss, H. Phase transitions in systems small enough to be clusters. *J. Chem. Phys.* **2003**, *118*, 340.
(66) Kožíšek, Z.; Demo, P. Influence of vapor depletion on nucleation rate. *J. Chem. Phys.* **2007**, *126*, No. 184510.
(67) Schmelzer, J. W. P.; Abyzov, A. S. Thermodynamic analysis of nucleation in confined space: Generalized Gibbs approach. *J. Chem. Phys.* **2011**, *134*, No. 054511.
(68) Philippe, T. Nucleation and superstabilization in small systems. *Phys. Rev. E* **2017**, *96*, No. 032802.
(69) Harmand, J. C.; Patriarche, G.; Glas, F.; Panciera, F.; Florea, I.; Maurice, J.-L.; Travers, L.; Ollivier, Y. Atomic step flow on a nanofacet. *Phys. Rev. Lett.* **2018**, *121*, No. 166101.
(70) Panciera, F.; Baraissov, Z.; Patriarche, G.; Dubrovskii, V. G.; Glas, F.; Travers, L.; Mirsaidov, U.; Harmand, J. C. Phase selection in self-catalyzed GaAs nanowires. *Nano Lett.* **2020**, *20*, 1669.
(71) Marnauza, M.; Tornberg, M.; Mårtensson, E. K.; Jacobsson, D.; Dick, K. A. In situ observations of size effects in GaAs nanowire growth. *Nanoscale Horiz.* **2023**, *8*, 291.
(72) Glas, F.; Dubrovskii, V. G. Energetics and kinetics of monolayer formation in vapor-liquid-solid nanowire growth. *Phys. Rev. Materials* **2020**, *4*, No. 083401.
(73) Glas, F.; Panciera, F.; Harmand, J. C. Statistics of nucleation and growth of single monolayers in nanowires: towards a deterministic regime. *Phys. Status Solidi RRL* **2022**, *16*, No. 2100647.
(74) Glas, F. Incomplete monolayer regime and mixed regime of nanowire growth. *Phys. Rev. Materials* **2024**, *8*, No. 043401.
(75) Glas, F.; Ramdani, M. R.; Patriarche, G.; Harmand, J. C. Predictive modeling of self-catalyzed III-V nanowire growth. *Phys. Rev. B* **2013**, *88*, No. 195304.
(76) Pishchagin, A.; Glas, F.; Patriarche, G.; Cattoni, A.; Harmand, J. C.; Oehler, F. Dynamics of droplet consumption in vapor−liquid−solid III−V nanowire growth. *Cryst. Growth Des.* **2021**, *21*, 4647.
(77) Mosiiets, D.; Genuist, Y.; Cibert, J.; Bellet-Amalric, E.; Hocevar, M. Dual-adatom diffusion-limited growth model for compound nanowires: Application to InAs nanowires. *Cryst. Growth Design* **2024**, *24*, 3888.
(78) Costigliola, L.; Heyes, D. M.; Schrøder, T. B.; Dyre, J. C. Revisiting the Stokes-Einstein relation without a hydrodynamic diameter. *J. Chem. Phys.* **2019**, *150*, No. 021101.
(79) Madelung, O. *Semiconductors: Data handbook*; Springer Science & Business Media (2004).
(80) Glas, F.; Harmand, J. C.; Patriarche, G. Why does wurtzite form in nanowires of III-V zinc-blende semiconductors ? *Phys. Rev. Lett.* **2007**, *99*, No. 146101.
(81) Ansara, I.; Chatillon, C.; Lukas, H. L.; Nishizawa, T.; Ohtani, H.; Ishida, K.; Hillert, M.; Sundman, B.; Argent, B. B.; Watson, A.; Chart, T. G.; Anderson, T. A binary database for III−V compound semiconductor systems. *Calphad* **1994**, *18*, 177.
(82) Dinsdale, A. T. SGTE unary database ver. 4.4. *Calphad* **1991**, *15*, 317.
(83) Cirlin, G. E.; Dubrovskii, V. G.; Sibirev, N. V.; Soshnikov, I. P.; Samsonenko, Yu. B.; Tonkikh, A. A.; Ustinov, V. M. The diffusion mechanism in the formation of GaAs and AlGaAs nanowhiskers during the process of molecular-beam epitaxy. *Semiconductors* **2005**, *39*, 557.
(84) Filho, M. A. M.; Hsiao, C.-L.; dos Santos, R. B.; Hultman, L.; Birch, J.; Gueorguiev, G. K. Self-induced core−shell InAlN nanorods: Formation and stability unraveled by ab initio simulations. *ACS Nanosci. Au* **2023**, *3*, 84.
(85) Filho, M. A. M.; Farmer, W.; Hsiao, C.-L.; dos Santos, R. B.; Hultman, L.; Birch, J.; Ankit, K.; Gueorguiev, G. K. Density functional theory-fed phase field model for semiconductor nanostructures: The case of self-induced core-shell InAlN nanorods. *Cryst. Growth Des.* **2024**, *24*, 4717.
(86) Dubrovskii, V. G.; Cirlin, G. E.; Kirilenko, D. A.; Kotlyar, K. P.; Makhov, I. S.; Reznik, R. R.; Gridchin, V. O. Instantaneous growth of single monolayers as the origin of core-shell $In_xGa_{1-x}N$ nanowires with bright red photoluminescence. *Nanoscale Horiz.* **2024**, *9*, 2360.
(87) Chen, X.; Le, N. Q.; Clancy, P. Diffusion-limited crystal growth of gallium nitride using active machine learning. *Cryst. Growth Des.* **2024**, *24*, 2855.
(88) Dubrovskii, V. G.; Shtrom, I. V.; Reznik, R. R.; Samsonenko, Yu. B.; Khrebtov, A. I.; Soshnikov, I. P.; Rouvimov, S.; Akopian, N.; Kasama, T.; Cirlin, G. E. Origin of spontaneous core-shell AlGaAs nanowires grown by molecular beam epitaxy. *Cryst. Growth Des.* **2016**, *16*, 7251.

https://doi.org/10.1021/acs.cgd.4c01338
Cryst. Growth Des. XXXX, XXX, XXX−XXX